International Journal of Power Electronics and Drive System (IJPEDS)
Vol. 17, No. 3, September 2026, pp. 2224~2246
ISSN: 2088-8694, DOI: 10.11591/ijpeds.v17.i3.pp2224-2246

Enhanced voltage control and load compensation for DFIG-based wind energy systems using a stator-side series converter

Preethicaa Ramesh[1], Sowmmiya Uthayakumar[1], Tole Sutikno[2,3], Vigna Kumaran Ramachandaramurthy[4]
[1]Department of Electrical and Electronics Engineering, SRM Institute of Science and Technology, Kattankulathur, India
[2]Faculty of Industrial Technology, Universitas Ahmad Dahlan, Yogyakarta, Indonesia
[3]Embedded System and Power Electronics Research Group, Yogyakarta, Indonesia
[4]Institute of Power Engineering, Universiti Tenaga Nasional, Selangor, Malaysia

Article Info

Article history:

Received Nov 24, 2025
Revised Jul 3, 2026
Accepted Aug 14, 2026

Keywords:

Doubly-fed induction generators
Load compensation
Power quality
Stator-side series converter
Voltage control

ABSTRACT

The increasing deployment of doubly-fed induction generator (DFIG)-based wind energy systems (WESs) requires effective voltage regulation and power-quality enhancement under varying operating conditions. This paper proposes a coordinated voltage regulation and load-compensation technique using a rotor-side converter (RSCR) and a stator-side series converter (SSSCR). The RSCR provides two-directional slip-power control through cascaded voltage and current control loops, while the SSSCR provides series voltage injection for voltage regulation and load compensation. The proposed system is developed in MATLAB/Simulink and validated using an OPAL-RT OP4512 real-time platform under variable wind speed, unbalanced and non-linear loading, and voltage sag/swell conditions. Quantitative results show reductions in overall current total harmonic distortion (THD) of 25.34% and 36.78% under non-linear and unbalanced load conditions, respectively. The voltage regulation error is reduced from 9% to 3%, while the settling time decreases from 0.24 s to 0.12 s under non-linear loading. The proposed configuration also reduces the voltage overshoot from 2.61% to 0.02% during speed transition. These results demonstrate the effectiveness of the coordinated RSCR–SSSCR configuration for simultaneous voltage regulation and load compensation.

Corresponding Author:

Sowmmiya Uthayakumar
Department of Electrical and Electronics Engineering, SRM Institute of Science and Technology
Kattankulathur, Chennai 603203, Tamil Nadu, India
Email: sowmmiyu@srmist.edu.in

NOMENCLATURE

Symbol	Definition	Unit	Symbol	Definition	Unit
P_m	: Mechanical power extracted from the wind turbine	W	v_{inj}	: Voltage injected by the SSSCR through the coupling transformer	V
c_1, c_2, c_3 c_4, c_5, c_6	: Empirical coefficients of the model	–	v_{SSSCR}	: SSSCR converter-side output voltage	V
ρ	: Air density	kg/m³	i_{rabc}	: Three-phase rotor current	A
v_w	: Wind velocity	m/s	v_{st}	: Stator terminal voltage	V
A	: Swept area of wind turbine blades	m²	v_g	: Grid voltage	V

Symbol	Definition	Unit	Symbol	Definition	Unit
R	: Turbine blade radius	m	m	: Converter modulation index	–
C_p	: Turbine power coefficient	–	v_{sabc}	: Three-phase stator voltage	V
Β	: Blade pitch angle	degree	Λ	: Tip-speed ratio	–
v_{sd}, v_{sq}	: Stator d- and q-axis voltage components	V	v_{sd}^*, v_{sq}^*	: Reference stator d- and q-axis voltages	V
ω_t	: Turbine angular speed	rad/s	v_{rd}, v_{rq}	: Rotor d- and q-axis voltages	V
v_{sd}, v_{sq}	: Stator d- and q-axis voltages	V	i_{sd}, i_{sq}	: Stator d- and q-axis currents	A
v_{rd}^*, v_{rq}^*	: Reference rotor d- and q-axis control voltages	V	i_{rd}, i_{rq}	: Rotor d- and q-axis current components	A
v_{rabc}^*	: Three-phase rotor reference voltage signals	V	i_{rd}^*, i_{rq}^*	: Reference rotor d- and q-axis currents	A
i_{rd}, i_{rq}	: Rotor d- and q-axis currents	A	ω_r	: Actual rotor angular speed	rad/s
ψ_{sd}, ψ_{sq}	: Stator d- and q-axis flux linkages	Wb	ω_s^*	: Reference synchronous angular speed	rad/s
ψ_{rd}, ψ_{rq}	: Rotor d- and q-axis flux linkages	Wb	e_ω	: Rotor speed error	rad/s
ω_s	: Synchronous/reference-frame angular speed	rad/s	ω_s	: Synchronous/reference-frame angular speed	rad/s
ω_r	: Rotor electrical angular speed	rad/s	θ_e	: Electrical reference-frame angle	rad
R_{str}	: Stator resistance	Ω	J	: Rotor moment of inertia	kg·m²
R_{rtr}	: Rotor resistance	Ω	B	: Friction/damping coefficient	N·m·s/rad
L_{str}	: Stator inductance	H	P	: Number of poles	–
L_{rtr}	: Rotor inductance	H	P_s	: Stator active power	W
L_{int}	: Interlinking (mutual) inductance	H	P_r	: Rotor active power	W
T_e	: Electromagnetic torque	N·m	s	: DFIG slip	–
T_m	: Mechanical torque	N·m	V_{dc}	: DC-link voltage (DCLV)	V
I_{dc}	: DC-link current	A	C_{dc}	: DC-link capacitance	F

1. INTRODUCTION

The rapid penetration of renewable energy (RE) into the power system network enables the modern power grids to meet the ever-increasing load demand and acts as solution for many stabilities related issues of grid. Among the various RE, wind energy systems (WES) are the most mature and widely deployed one owing to the environmental benefits, and economic viability. In specific, the variable speed, doubly-fed induction generator (DFIG)-WES are widespread with wide acceptance owing to its operation over a wide speed range, ruggedness, and dual power retrieval capability on both stator and rotor ends [1]. These capabilities allow improved energy capture and efficient grid integration, making DFIG systems a preferred choice in large-scale wind farms [2].

In modern power system networks, maintaining stable operation under fluctuating wind conditions is a critical requirement. The integration of wind energy systems into power grids can introduce voltage fluctuations, harmonic disturbances, and voltage asymmetries, which can adversely affect power quality and system stability [3], [4]. Additionally, the existence of unbalanced and non-linear loads at the point of common coupling (PCC) exacerbates power quality issues [5]. During such conditions, there arises a need for DFIG systems to perform both voltage injection and load compensation along with mitigation of power quality issues. Moreover, during the grid integration of WES at the upstream, to manage the trade-off between voltage injection and load compensation, a simultaneous operation of all the above in a single unified setup without any additional component or equipment becomes the need of the problem.

Under grid disturbances, DFIG-based WESs are sensitive to voltage variations due to their partial-scale power converter structure, where only the rotor is directly controlled while the stator remains connected to the grid. The system is greatly affected with power quality issues and also suffers from stability issues due to unbalances in voltages and distorted currents [6]–[8]. Upon coupling with power grids, voltage fluctuations can be addressed using an additional dynamic voltage restorer (DVR) [9], [10] to improve voltage quality and system stability. Conventionally, a two-stage back-to-back connected converter structure is deployed in DFIG based WECS and the grid side connectivity is shunt-based concentrating on only the load compensation [11]. The unified power quality conditioner (UPQC) structure and the two-stage back-to-back connected converters proposed [12], [13], with one converter performing load compensation and another converter performing voltage regulation, having two different operations performed by two different converters leading to costlier and complex control system [14]–[16]. To cope up with simultaneous voltage regulation and load compensation, dual-converter structure is proposed in [17] having different control schemes leading to complex control schemes and large DC link requirement. In this work, the stator side converter itself acts as one unified converter performing voltage regulation primarily and compensates the load to a greater extent overcoming the setbacks of the other conventional structures in the literature. The proposed configuration uses an RSCR for rotor-side power control and an SSSCR connected in series with the DFIG stator through an injection transformer for controlled voltage injection and load compensation, thereby reducing the converter cost.

The control scheme coordinates cascaded RSCR voltage/current loops with SSSCR power-based compensation. However, the cost of implementation is high. Several control strategies are also adopted to address the regulation issues. The control strategy proposed in [18], [19] for DFIG systems addresses unbalanced grid voltages and demonstrated that negative-sequence voltage components adversely affect rotor currents, electromagnetic torque, and power oscillations. Similarly, the AC voltage and reactive power control strategies for DFIG-based wind farms connected to compensated and weak networks are discussed in [20]–[22]. The study revealed that improper reactive power management can intensify sub-synchronous resonance phenomena and compromise system stability. Apart from voltage-related issues, harmonic distortion remains a major concern in DFIG-based wind energy systems due to the extensive use of electronic power conversion systems. The comprehensive review of suppressing harmonic techniques for grid-integrated DFIG systems in [23] highlighted that converter switching actions, nonlinear loads, and grid disturbances contribute significantly to harmonic generation. Intelligent and adaptive controllers with fault ride through capability are proposed in [24] to indicate the necessity for voltage recovery, improved transient stability, and enhanced fault tolerance. The stability degradation and resonance-related issues [25]–[27] are also addressed using controllers that define boundary framework and demonstrated that improper controllers may lead to oscillatory behavior. The findings to address the power quality issues, voltage injection during faults, regulation of voltage and frequency, mostly have restricted to address any one of the problem statements and not all of them on one unified approach. Moreover, in DFIG based WES, the grid connected converter is intended to perform load compensation only and is the most widely reported structure.

The above studies demonstrate the importance of coordinated voltage regulation, load compensation, and power-quality enhancement but fail to address them in a simultaneous manner in DFIG-based WESs. Furthermore, the control schemes involve complex mathematical formulations leading to control complexities during implementation. The entire state of art along with research gaps are depicted in Figure 1 for easier reference.

In this work, a capricious speed, DFIG-based WES is proposed to provide simultaneous voltage injection and load compensation under grid voltage disturbances and load variations. The system employs two converters: one interfaced to the rotor as rotor side converter (RSCR) while the other is linked to the stator as stator side series converter (SSSCR). The main merit is the connectivity in the stator in series fashion so as to inject voltage and compensate for reactive power through a unified control scheme exerted through a current controlled, reference current generation technique. The proposed control strategy supports the system voltage and load during unbalanced and non-linear loading at the point of common coupling (PCC). A simplified, coordinate transformation less, current controlled, reference current computation technique is proposed for SSSCR to exert, i) two-directional rotor slip-power exchange, ii) load compensation, iii) regulation of voltage and frequency at the stator, iv) reduced THD, and v) enhanced voltage support during sag/swell–all with one single unified system/approach claims to be the main merit of this work. The entire system is validated through computer-based simulation with MATLAB software and real time through Opal-RT (OP4512) based hardware-in-loop (HiL) approach. The major contributions of the work reported in this paper are

- Design and development of variable speed, DFIG based WES that would operate under various wind velocities, various loads – unbalanced and nonlinear loads and voltage sag and swell conditions.
- Deployment of coordinated, cascaded, outer voltage and inner current loop structure for RSCR and simplified, coordinate transformation less current controlled, reference current computation technique for SSSCR.
- Validation of multiple objectives: i) two-directional slip-power exchange, ii) load compensation, iii) regulation of voltage and frequency at the stator, iv) reduced THD, and v) enhanced voltage support during sag/swell – all with one single unified system/approach.
- Comprehensive investigation through computer-based simulation using MATLAB software and real time validation through Opal-RT (OP-4512) based hardware-in-loop (HiL) approach.

The structure of this article is organized as follows: i) The fundamental architecture of the proposed system is outlined in section 2; ii) Detailed modelling of the components in the system is elaborated in section 3; iii) The control methodologies for stator side series converter (SSSCR) and rotor side converter (RSCR) are provided in section 4; iv) The computer simulation-based performance results and real-time Hardware-in-Loop (HiL) validation are presented in section 5; and v) The main findings and contributions of this paper are furnished in section 6.

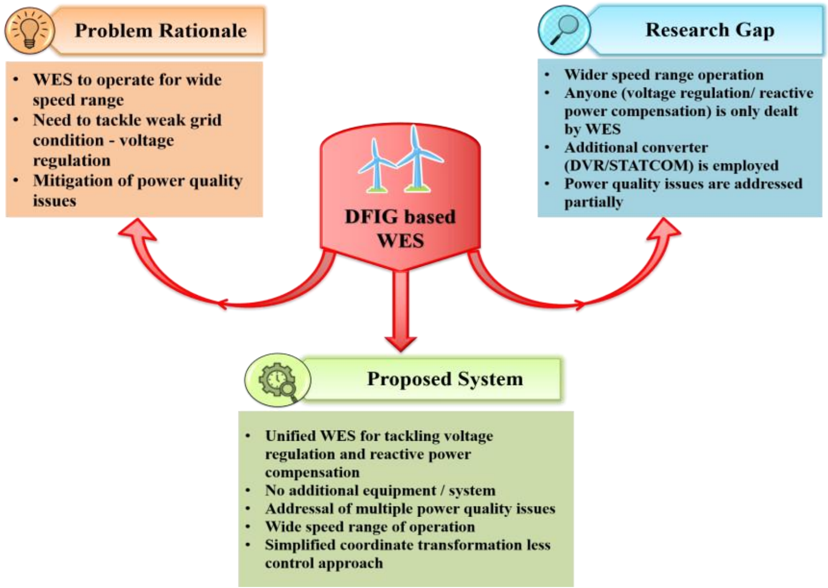

Figure 1. State-of-art for the proposed work

2. SYSTEM FRAMEWORK

A variable speed WES employing DFIG as the wind generator is proposed for the study and the same is depicted in Figure 2. The gear arrangement links the DFIG to the wind turbine. The DFIG is rated to about 1 kW and delivers a stator voltage of 575 V and a 1.75 kVA transformer (T_1) steps up the voltage from 575 V to 25 kV. The transmitted power travels along a 30 km transmission line to reach the 25 kV bus. At transformer T_2, the voltage is again stepped up to 120 kV to join the utility grid. The rotor end is interfaced with the rotor side converter (RSCR), and the DC end is linked to a DC-bus energy-storage capacitor. This DC terminal is then tied to the stator side series converter (SSSCR), whose AC end is connected in series with the generator stator. The SSSCR is connected to the 575 V bus, which is designated as the point of common coupling (PCC). The DC-link capacitor maintains a constant V_{dc} to accommodate power fluctuations arising from variations in generator output and grid disturbances.

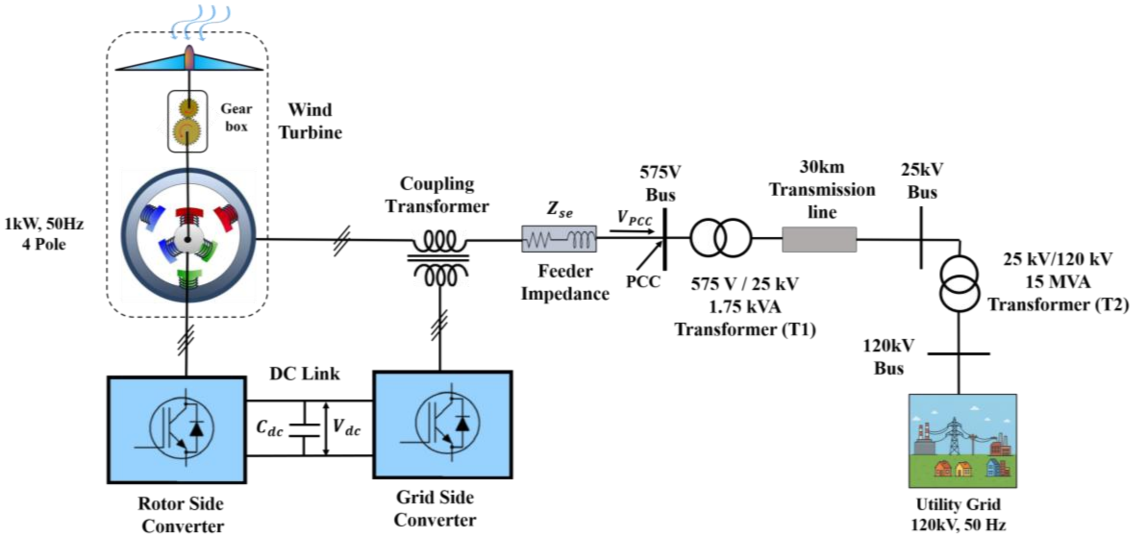

Figure 2. Single-line schematic of the proposed wind energy system

The load parameters used for the scaled 1 kW system are selected consistently with the rated operating conditions. For the linear-load condition, a balanced three-phase RL load comprising a resistance 300 Ω and an inductance of 0.3 H is considered. For the nonlinear-load condition, a three-phase diode-bridge rectifier load with a resistive load of 110 Ω and a filter capacitance of 0.001 F on DC-side is employed. The system specifications are provided in the Table 1.

The power quality issues, which are usually caused by various anomalies and unexpected events that happen with the electrical supply including unbalanced and non-linear loads, significantly impacts the proposed network's efficiency, dependability, and performance. Some of the main reasons for these problems are using nonlinear loads, fluctuations in voltage, electromagnetic interference, and incorporating renewable energy sources. The SSSCR is regulated utilizing simplified current controlled reference current controlled reference current generation technique and aims at simultaneous compensation load and voltage regulation at the PCC. Coordinated, voltage and current loops in a cascaded configuration are used to control the RSCR. The control methods are explained in more detail in the subsequent sections. The parameters are implemented in the OPAL-RT real-time simulation platform (OP4512) through the hardware-in-loop (HiL) approach to validate the outcomes of the computer simulation.

Table 1. System configuration specifications

	Parameters	Ratings		Parameters	Ratings
DFIG	Rated power	1 kW	Feeder	Feeder impedance	0.05+j1.57 Ω
	Rated voltage	0.575 kV	DC Link	DC bus voltage	1150 V
	Frequency	50 Hz		DC bus capacitance	220 μF
	No. of poles	4	Converters	Snubber resistance	1000 Ω
	Interlinked inductance	282.64 μH		Snubber capacitance	0.1 μF
	Stator-side resistance	0.00074 Ω		On-state resistance	1 mΩ
	Stator-side inductance	15.60 μH		Switching frequency	5 kHz
	Rotor-side resistance	0.05879 Ω			
	Rotor-side inductance	7.54 μH			
	Inertia constant	0.0139 kg·m²			
	Friction factor	0.01 N.m.s/rad			

3. MODELLING OF THE SYSTEM

The dynamic behavior of the WES is described through detailed mathematical models of its constituent subsystems, ensuring reproducibility and analytical clarity.

3.1. Wind turbine

The wind turbine model is formulated based on aerodynamic power extraction, where the mechanical power depends on wind velocity, air density, and turbine characteristics. The coefficient of performance is expressed as a nonlinear function of tip-speed ratio and pitch angle, enabling realistic emulation of wind variations. The wind energy captured by the turbine is computed in (1) with ρ (1.225 kg/m³), indicating the specific density of air, V_w indicating the wind velocity, denotes the swept area of the wind turbine blades, which is 4.08 m² and C_{eff} indicating the coefficient of turbine power which is computed in (2) and (3). The corresponding turbine blade radius, R is approximately 1.14 m.

$$P_m = 0.5C_{eff}(\lambda_0,\beta)\rho A V_w^3 = 0.5C_{eff}(\lambda_0,\beta)\rho\pi r2V_w^3 \quad (1)$$

$$\lambda_0 = \frac{W_t R}{V_w} \quad (2)$$

$$C_{eff}(\lambda_0,\beta) = C_1(\frac{C_2}{\lambda_0} - C_3\beta - C_4)e^{-C_5/\lambda_0} + C_6\lambda_0 \quad (3)$$

In this expression, β and λ_0 corresponds to the blade pitch angle and tip speed ratio respectively. The coefficient constants are C_1-C_6 are 0.5234, 110, 0.6, 4.37, 23, 0.0036 respectively [28].

3.2. Wind generator - DFIG

The DFIG model is developed in the synchronous reference frame model incorporating stator and rotor voltage equations, flux-linkage relationships, and electromagnetic torque dynamics. This formulation captures the electromechanical coupling and allows independent control of active and reactive power through rotor currents. The voltage equations of the DFIG with flux linkage in (4)-(7) are as:

$$V_{ds} = R_{str}.I_{ds} + \rho\psi_{ds} - \omega\psi_{qs},\ \ V_{qs} = R_{str}.I_{qs} + \rho\psi_{qs} + \omega\psi_{ds} \quad (4)$$

$$V_{dr} = R_{rtr}.I_{dr} + \rho\psi_{dr} - (\omega - \omega_r)\psi_{qr}\ ,V_{qr} = R_{rtr}.I_{qr} + \rho\psi_{qr} + (\omega - \omega_r)\psi_{dr} \quad (5)$$

$$\psi_{ds} = L_{str}.I_{ds} + L_{int}.I_{dr},\ \psi_{qs} = L_{str}.I_{qs} + L_{int}.I_{qr} \quad (6)$$

$$\psi_{dr} = L_{int}.I_{ds} + L_{rtr}.I_{dr},\ \psi_{qr} = L_{int}.I_{qs} + L_{rtr}.I_{qr} \quad (7)$$

where voltages in the dq-axis of stator are represented by V_{ds} and V_{qs} and in dq-axis of rotor by V_{dr} and V_{qr}, currents in the dq-axis of stator by I_{ds} and I_{qs}, and dq-axis of rotor by I_{dr} and I_{qr}, flux linkages in the dq-axis of stator by ψ_{ds} and ψ_{qs}, and dq-axis of rotor by ψ_{dr} and ψ_{qr}, ω is the frame's angular speed, the speed of the electrical rotor is denoted as ω_r, L_{str} is the inductance of the stator-side , L_{rtr} is the inductance of the rotor-side, L_{int} is the interlinked inductance, R_{rtr} is the resistance in the rotor and R_{str} is the resistance in the stator. The electrical torque as well as the equation that describes the rotor rotation is given in (8).

$$T_e = \left(\frac{3}{2}\right)\left(\frac{P}{2}\right)\left(\psi_{ds} I_{qs} - \psi_{qs} I_{ds}\right) \quad (8)$$

The mechanical dynamics of the DFIG can be represented by the torque-balance equation in (9), which relates the rotor acceleration to the mechanical torque, electromagnetic torque, and mechanical damping torque. The equation provides the mechanical basis for the turbine-generator dynamics.

$$J\frac{d\omega_r}{dt} = (T_m - T_e - B\omega_r) \quad (9)$$

Where J denotes the rotor moment of inertia (kg·m²), ω_r corresponds to the rotor angular speed (rad/s), and $\frac{d\omega_r}{dt}$ represents the rotor angular acceleration (rad/s²), T_m and T_e represents the mechanical torque (Nm) and electromagnetic torque (Nm), B is the friction coefficient (Nm), and the term $B\omega_r$ represents the friction/damping torque (Nm).

The DFIG is operated over a variable-speed regime spanning the synchronous speed to accommodate wind-speed variations and to facilitate sub-synchronous as well as super-synchronous operating conditions [28]. The total power delivered by the DFIG is given in (10).

$$P_{to} = P_{sp} + P_{rp} = (1 + |s|)\, P_{sp} \quad (10)$$

For a DFIG, $P_{rp} = -s\, P_{sp}$, where $P_{sp}\ and\ P_{rp}$ corresponds to the stator and the rotor active power respectively, with the sign determined by the adopted power-flow convention. Hence, for super synchronous operation.

3.3. Modelling of RSCR and SSSCR

The power electronic converters (RSCR and SSSCR) are represented using state-space equations incorporating dq-axis currents and DC-link voltage (DCLV) dynamics. The rotor side converter (RSCR) along with stator side series converter (SSSCR) are utilized for slip power recovery are designed using (11).

$$\begin{bmatrix} \frac{dI_{xd}}{dt} \\ \frac{dI_{xq}}{dt} \\ \frac{dV_{dc}}{dt} \end{bmatrix} = \begin{bmatrix} 0 & \omega_x & \frac{-u_{xd}}{L_{se}} \\ -\omega_x & 0 & \frac{-u_{xq}}{L_{se}} \\ \frac{u_{xd}}{C_{dc}} & \frac{u_{xq}}{C_{dc}} & 0 \end{bmatrix} \begin{bmatrix} I_{xd} \\ I_{xq} \\ V_{dc} \end{bmatrix} + \begin{bmatrix} \frac{1}{L_{se}} & 0 & 0 \\ 0 & \frac{1}{L_{se}} & 0 \\ 0 & 0 & -\frac{1}{C_{dc}} \end{bmatrix} \begin{bmatrix} V_{xd} \\ V_{xq} \\ I_{dc} \end{bmatrix} \quad (11)$$

Where, L_{se} is the impedance in the feeder, V_{dc} is the voltage in the dc connection, I_{dc} is the current in the dc connection, ω_x is the angular speed u_{xd}, u_{xq} are the switching pulses and V_{xd} and V_{xq} represent the d–q components of the voltage at the converter terminals and. I_{xd}, I_{xq} are input currents of the converters on the AC end where the subscript x serves as a common notation denoting either r for the RSCR or s for the SSSCR.

$$V_{xcr} = \frac{m_{index} \cdot V_{dc}}{2\sqrt{2}} \quad (12)$$

Where V_{xcr} represents the RMS value of the fundamental phase voltage of converter x, the subscript $x$denotes either the RSCR ($x = r$) or the SSSCR ($x = s$). V_{dc} is the DC-bus voltage and m_{index} signifies the modulation index of the sinusoidal pulse-width modulation (SPWM) scheme [29].

3.4. DC link dynamics

The DC-link capacitor is modelled to maintain energy balance between the converters, ensuring stable operation during transient conditions. The DC link is positioned between SSSCR and RSCR through an intermediary energy storage component. A capacitor (C_{dc}) is typically employed in the DC link that smooths out voltage fluctuations, ensuring stable DC voltage during power exchange [30]. It maintains power balance between RSCR and SSSCR, enabling efficient energy transfer. The dynamics of the DC bus voltage are described by (13).

$$C_{dc}\frac{dV_{dc}}{dt} = I_{rdc} - I_{gdc} \tag{13}$$

Where C_{dc} is the DC-link capacitance, I_{rdc} represents the DC current from the RSCR, I_{gdc} represents the DC current to the SSSCR. During extended voltage sags or swells, the energy storage dynamics becomes critical. In a capacitor-based storage system, the current through the DC link (I_{dc}) can be described in (14).

$$I_{dc} = C_{dc}\frac{dV_{dc}}{dt} \tag{14}$$

3.5. Coupling transformer

An injection transformer is employed to interface the SSSCR output with the stator terminals, enabling compensation voltage injection during disturbances. This transformer ensures voltage level matching between the converter and the grid. The correlation between the injected voltage V_{inj} and the voltage at the converter output V_{ssscr} is given in (15).

$$V_{inj} = N \cdot V_{ssscr} \tag{15}$$

Where N is the coupling transformer's turn ratio. This facilitates efficient injection of the compensating voltage under symmetrical and asymmetrical disturbances [31].

3.6. Modelling of AC grid

The AC transmission system interfaced to the stator terminal of the DFIG is modelled using a series impedance to represent line losses and capacitive effects. The SSSCR, coupled in series with the stator through the coupling transformer, plays a key role in dynamic voltage compensation under grid disturbances. At the PCC, the stator terminal voltage is determined by the combined effects of the low-voltage bus, the transmission line drop, and the voltage injected by the SSSCR, as described in (16).

$$V_{st} = V_{PCC} - Z_{se} \cdot I_{PCC} + V_{inj} \tag{16}$$

Where V_{st} is the stator-side terminal voltage, V_{PCC} is the PCC voltage of the grid, Z_{se} is the series impedance at the transmission line, I_{PCC} represents the line current at the PCC, and V_i is the voltage injected by the SSSCR through the coupling transformer [32].

4. CONTROL METHODOLOGY FOR RSCR AND SSSCR

The system employs two converters, RSCR and SSSCR, to achieve objectives; i) two-directional rotor slip-power exchange, ii) load compensation, iii) regulation of voltage and frequency at the stator, iv) reduced THD, and v) enhanced voltage support during sag/swell – all with one single unified system/approach.

4.1. Control scheme of RSCR

The overall control scheme for RSCR is illustrated in Figure 3 and it employs cascaded control scheme with an internal loop for controlling rotor current and external loop to regulate the stator voltage. The 3φ stator voltages V_{sabc} are transformed from abc frame into 2φ dq-orthogonal parameter V_{ds} and V_{qs} and are compared with their dq reference voltages V_{ds}^* and V_{qs}^* to get voltage error values V_{dser} and V_{qser} are given in (17). The reference V_{ds}^* is set as 469 V (RMS).

$$V_{dser} = V_{ds}^* - V_{ds}\ ;\ V_{qser} = V_{qs}^* - V_{qs} \tag{17}$$

The resultant voltage errors are then processed by proportional–integral (PI) controllers to generate the reference rotor current components I_{dr}^* and I_{qr}^* using gains $K_{p,v}$ and $K_{i,v}$ as shown in (18) and (19). The proportional and integral gains of the voltage controller are represented by parameters $K_{p,v}$ and $K_{i,v}$, respectively. The voltage control errors obtained from the deviation between the measured and reference values are fed to the PI controllers and the values of the loop gains are determined according to the Zeigler – Nichols tuning approach, which delivers the overall gain K_u=1.8 and ultimate period P_u= 0.06s. Using this tuning technique, the voltage-loop PI gains $K_{p,v}$ and $K_{i,v}$ are determined as 0.9 and 20, respectively, using $K_{p,v} = K_u/2$, $T_i = P_u/1.2$, and $K_{i,v} = 1/T_i$.

$$I_{dr}^* = K_{p,v}(V_{dser}) + K_{i,v}\int (V_{dser})dt \tag{18}$$

$$I_{qr}^* = K_{p,v}(V_{qser}) + K_{i,v}\int (V_{qser})dt \tag{19}$$

Where the terms I_{dr}^{*} and I_{qr}^{*} represent the resultant rotor current references in the dq reference frame. The 3φ rotor currents I_{rabc} are transformed from abc frame into 2φ dq-orthogonal parameter I_{dr} and I_{qr} by implementing park transformation which are compared with the outer loop resultant dq reference currents I_{dr}^{*} and I_{qr}^{*} to calculate current errors I_{drer} and I_{qrer} is shown in (20).

$$I_{drer} = I_{dr}^{*} - I_{dr}\ ;\ I_{qrer} = I_{qr}^{*} - I_{qr} \tag{20}$$

These resultant current errors are regulated using the PI controllers to generate the reference control rotor voltages V_{dr}^{*} and V_{qr}^{*} as shown in (21) and (22). Similar to the voltage loop, the PI gains for the current loop are also designed and are $K_{p,i}$ and $K_{i,i}$ are 0.6 and 10 respectively.

$$V_{dr}^{*} = K_{p,i}(I_{drer}) + K_{i,i}\int (I_{drer})dt \tag{21}$$

$$V_{qr}^{*} = K_{p,i}(I_{qrer}) + K_{i,i}\int (I_{qrer})dt \tag{22}$$

Where the terms V_{dr}^{*} and V_{qr}^{*} represent the resultant reference control rotor voltages in the d- and q-axes, respectively. To achieve proper synchronization, a speed feedback loop is added to this loop by contrasting the rotor speed response ω_r against the reference synchronous speed ω_r^{*}. The resulting error ω_{err} is then used to provide the necessary angular signals θ for synchronization as shown in (23).

$$\omega_{err} = \omega_r^{*} - \omega_r\ ;\ \theta = \int \omega dt \tag{23}$$

Where the symbol ω_r denotes the angular rotor speed (rad/s), ω_r^{*} is the reference synchronous speed and ω_{err} is the resultant speed error. The inverse of the park transformation is applied to the control voltages V_{dqr} and angle θ, converts them into the abc frame and produces the voltage signals V_{rabc} which are fed to the RSCR by converting them into PWM signals by fixed frequency mode with a switching frequency of 5 kHz. This closed-loop vector control approach ensures that the rotor current references are tracked accurately and improves the system's performance in both normal and disturbed conditions.

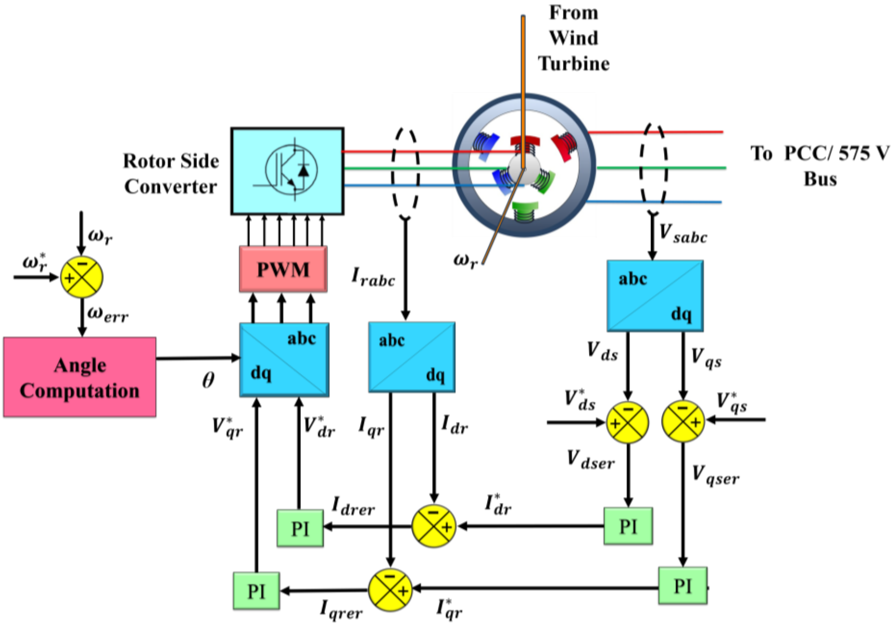

Figure 3. Schematic of RSCR control scheme

4.2. Control scheme of SSSCR

The control scheme for the stator side series converter (SSSCR) is illustrated in Figure 4 and it functions primarily as a series voltage regulator at the PCC, especially under non-linear and unbalanced loads. The SSSCR compensates during disturbances by injecting a series voltage and also performs load compensation at the PCC, ensuring that the voltage remains at its nominal value. To exert the above, a current controlled reference generation technique is employed that mitigates various voltage irregularities such as phase unbalances, non-linearities, voltage sags and swells.

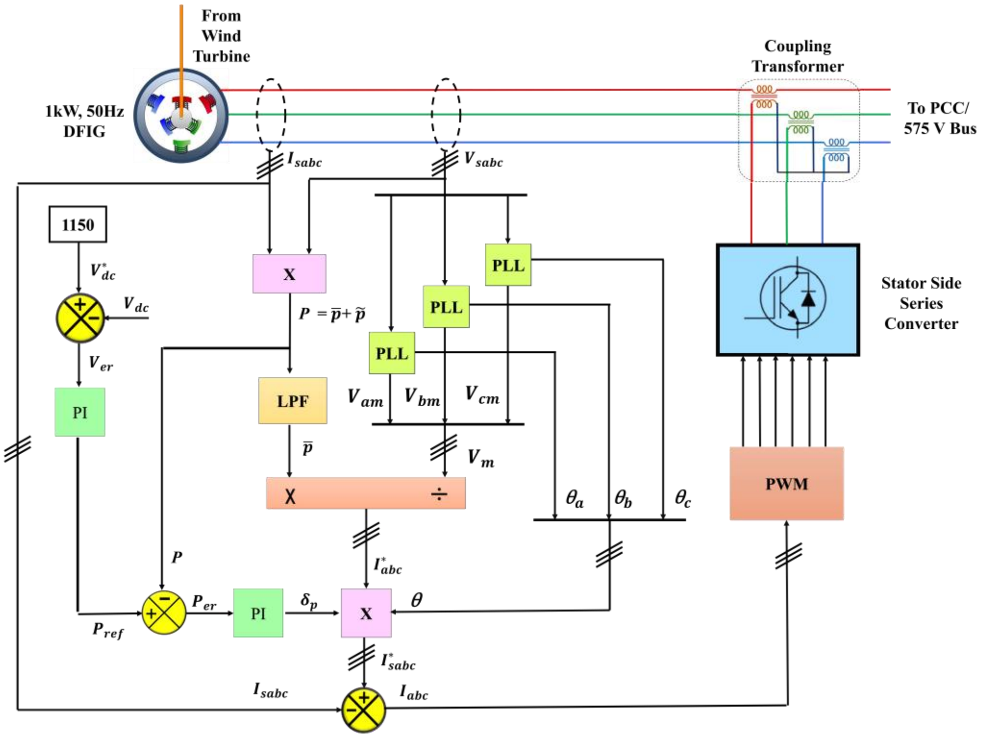

Figure 4. Schematic of SSSCR control scheme of the proposed system

The control scheme decomposes the instantaneous three-phase quantities and generates the total real power which is a culmination of average and oscillatory real powers as in (24) and (25) respectively.

$$P = v_a i_a + v_b i_b + v_c i_c \tag{24}$$

$$P = \bar{p} + \tilde{p} \tag{25}$$

To obtain the average real power, a low pass filter (LPF) is executed to the total power and the average real power is subsequently used with stator voltage to get the reference current I^*_{abc} as resultant as given in (27). The LPF used to extract the average power component is implemented as a fifth-order Butterworth low-pass filter configured for a cutoff frequency of 30 Hz. Since the dominant power oscillation occurs at the frequency corresponding to the second harmonic (100 Hz for a 50 Hz system), the 30 Hz cutoff effectively attenuates the oscillatory component and extracts the average power component. A fifth-order LPF was adopted to achieve an improved trade-off between filtering performance and dynamic response. The filter parameters were determined through simulation studies to minimize phase delay while maintaining accurate extraction of the average power component required for compensation.

$$\bar{p} = LPF(P) \tag{26}$$

The oscillatory power component $\tilde{p}$ represents the disturbances caused by voltage unbalance and harmonic components, which are compensated by the SSSCR. The measured three-phase stator voltages V_{sabc} are applied to a phase-locked loop (PLL), which estimates the grid phase angle $\theta$and extracts the fundamental positive-sequence voltage magnitude V_m. The estimated voltage magnitude V_m is subsequently utilized to compute the reference compensation current, which is expressed in (27).

$$I^*_{abc} = \frac{\bar{p}}{v_m} \tag{27}$$

Where I_{abc}^* denotes the three-phase reference compensation current to be injected by the SSSCR, and v_m represents the voltage magnitude. The DCLV of the back-to-back converter is maintained at its reference value through an outer voltage control loop. The measured DCLV V_{dc} is compared with its reference value V_{dc}^*, and the resulting voltage deviation is processed through a PI controller. The PI controller subsequently generates the reference active-power component P^* is expressed in (28) and (29).

$$V_{er} = V_{dc}^* - V_{dc} \quad (28)$$

$$P_{ref} = K_p(V_{er}) + K_i \int (V_{er})dt \quad (29)$$

To regulate the active power flow, a PI controller processes the error between the regulated reference signal of the active power and the measured regulated active power to generate the control signal δ_p. The PI controller gains of the active power control loop are selected using Zeigler-Nichols tuning approach as mentioned in Section 4.1 and the controller gains are given in Table 2. The tuning objective is to achieve fast active-power regulation, minimum overshoot, negligible steady-state error, and stable converter operation. The active power error is calculated using the (30) and (31).

$$P_{er} = P_{ref} - P \quad (30)$$

$$\delta_p = K_p(P_{er}) + K_i \int (P_{er})dt \quad (31)$$

Where P_{er} represents the active-power error signal, P_{ref} is the reference active power, P is the measured instantaneous active power and δ_p denotes phase shift in the modulating signals that is required for the effective regulation. The parameters K_p and K_i denote the proportional and integral gains of the active-power controller, respectively. To determine the phase angle, the stator voltage is aligned utilizing a PLL to extract the grid angle $\theta = \omega t$ from the stator voltage V_{sabc}. The symbol θ is then combined with δ_p and i_{abc}^* to get the reference/modulating waveform of the stator current i_{sabc}^*. This is then evaluated against the actual signal of the stator current i_{sabc}. The reference current i_{sabc}^* is differenced with the measured current i_{sabc}, and the resulting error is processed and fed to the controller as in (32).

$$i_{abc} = i_{sabc}^* - i_{sabc} \quad (32)$$

The quantities i_{sabc}^* and i_{sabc} denote the reference and measured three-phase currents, respectively, and i_{abc} represents the current error. A PWM controller processes the resultant error signal with a switching frequency of 5kHz and a sampling time of 5 µs so as to generate the PWM signals for SSSCR.

The stability of the controllers employed in the above control schemes are validated through frequency response analysis – Bode plots as shown in Figures 5(a)-5(e). Increasing the proportional and integral gains enhances the controller bandwidth by shifting the crossover frequency to higher values while maintaining stable high-frequency characteristics. With this note, the plots are analyzed, and suitable gains that ensure stability are deployed in the control. The RSCR voltage and current controllers exhibit consistent magnitude and phase responses over the investigated gain ranges, indicating robust loop dynamics and sufficient stability margins as shown in Figures 5(a) and 5(b). Similarly, the SSSCR power controller, PLL, and DC voltage loop demonstrate improved bandwidth with increasing controller gains while preserving stable phase characteristics as in Figures 5(c), 5(d), and 5(e). Based on this analysis, the final controller parameters as listed in Table 2 are selected as ($K_{p,v}$ = 0.9, $K_{i,v}$ = 20) for the RSCR voltage loop, ($K_{p,i}$ = 0.6, $K_{i,i}$ = 10) for the RSCR current loop, (K_p = 8, K_i = 100) for the SSSCR power controller, and ($K_{p,PLL}$ = 2, $K_{i,PLL}$ = 75) for the PLL. These gain values provide positive gain and phase margins while achieving a suitable compromise between bandwidth, transient response, overshoot, and settling time, thereby indicating the stability of the system. The controller tuning parameters and frequency-response characteristic are given in Table 2.

Table 2. Controller tuning parameters and frequency-response characteristic

Controller	Kp	Ki	GM (dB)	PM (°)	ω_{gc} (rad/s)	f_{gc} (Hz)	ω_{pc} (rad/s)
RSCR voltage loop	0.9	20	32	111	17.5	2.8	185
RSCR current loop	0.6	10	33.5	101	30	4.8	183
SSSCR power controller	8	100	17	57	26	4.1	95
PLL controller	2	75	27	71	29	4.6	138
DC voltage loop control	4	80	40	70	81.4	13	239

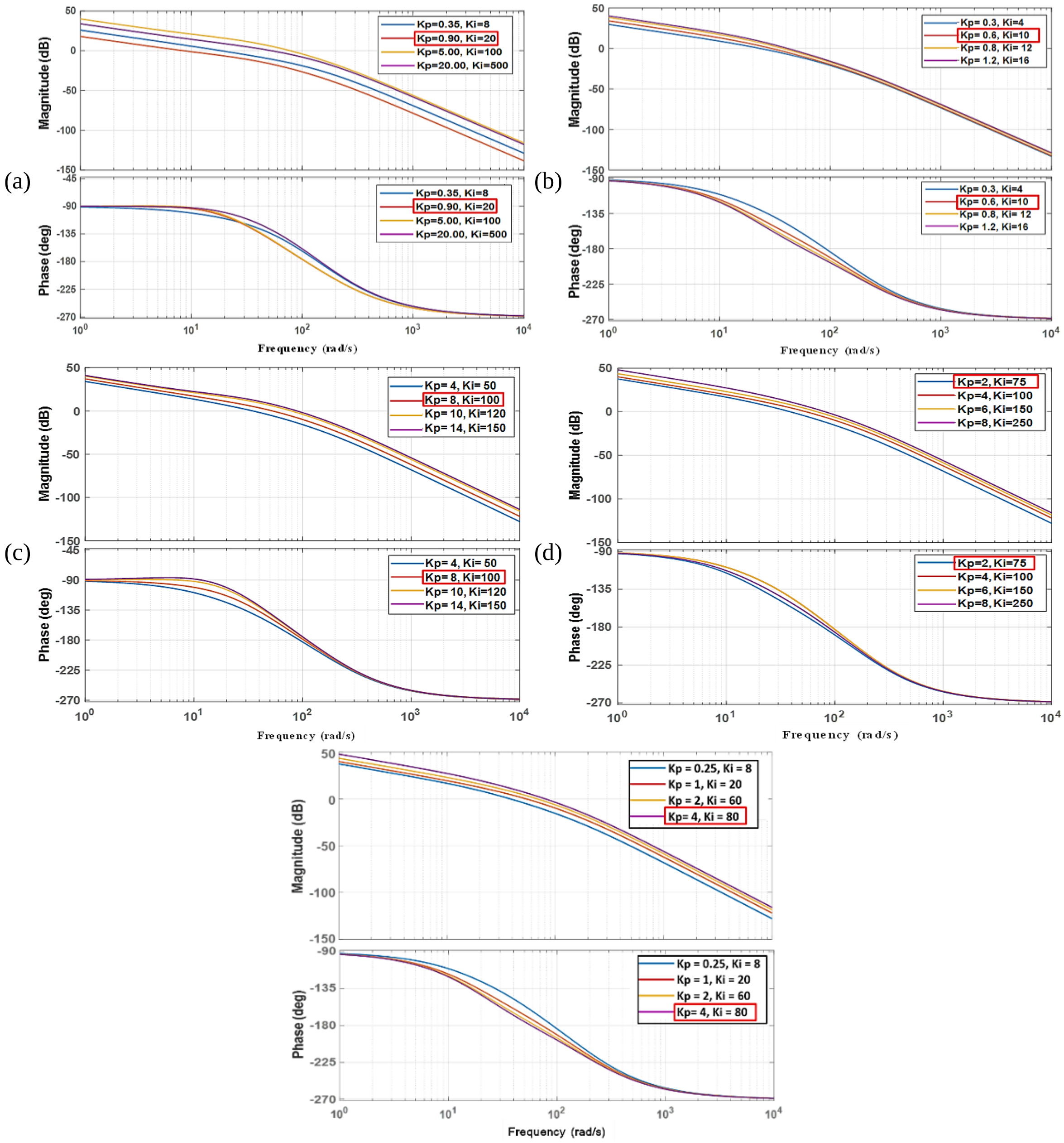

Figure 5. Frequency response for PI controller gain values: (a) RSCR voltage loop, (b) RSCR current loop, (c) SSSCR power controller, (d) SSSCR PLL controller, and (e) DC voltage loop controller

5. COMPUTER SIMULATION AND HARDWARE-IN-THE-LOOP (HiL) EVALUATION

The system is developed in MATLAB/Simulink R2024a to evaluate its dynamic performance under different operating conditions. To validate its real-time implementation, the simulation model is executed on an OPAL-RT OP4512 hardware-in-the-loop (HIL) platform. The OPAL-RT OP4512 is an FPGA-based real-time simulation platform with high computational performance specifically engineered for the rapid prototyping and closed-loop testing of power electronics and energy conversion systems [33]. The OP4512 real-time simulator incorporates a Xilinx Artix-7 XC7A100T FPGA, selected for its parallel processing architecture and deterministic execution capability, enabling high-speed implementation of real-time control algorithms. The FPGA architecture enables simultaneous implementation of the computationally intensive functions required by the proposed DFIG controller. The FPGA resources, comprising 101,440 logic cells, 240 DSP slices, and 4.9 MB of Block RAM provides adequate computational capacity to execute within a 5 µs sampling interval, ensuring low computational latency, deterministic timing, and accurate real-time control of the RSCR and SSSCR under varying wind, load, and grid disturbance conditions.

The simulated model and the controller communicate through the analogue output (2B) and analogue input (2A) channels, where the analogue output signals are looped back as controller feedback. The model is executed using the RT-LAB environment in a Master–Slave architecture, enabling closed-loop real-time operation. The analogue signals are appropriately scaled to emulate hardware interfacing, while the controller operates with a sampling time of 5 µs, satisfying the real-time requirements of the proposed control scheme.

The HIL setup is configured using RT-LAB, enabling real-time model execution, parameter tuning, and signal monitoring. A Tektronix MSO58B 5-BW-350 mixed signal oscilloscope (MSO), featuring a 350 MHz bandwidth and a maximum sampling rate of 6.25 GS/s, is used to capture and record key electrical waveforms and converter switching signals for performance evaluation. The schematic and experimental implementation of the HIL platform is presented in Figures 6(a) and 6(b), respectively.

(a)

(b)

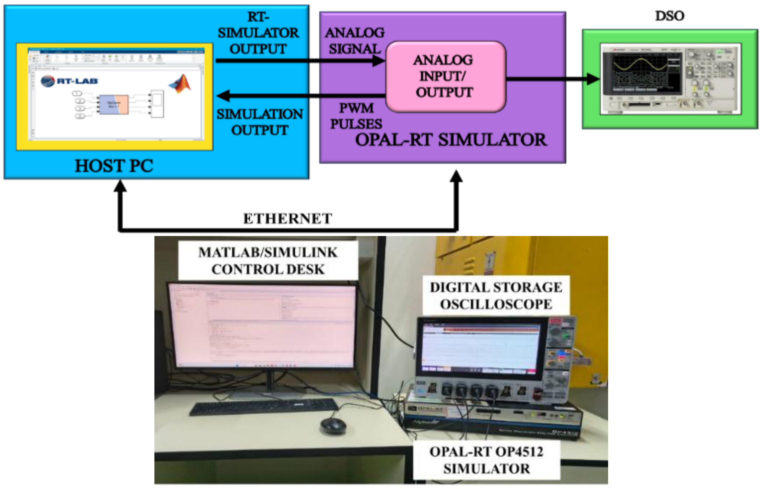

Figure 6. Hardware-in-the-loop setup: (a) schematic and (b) photograph

5.1. Dynamic response of the system with varying wind speeds

The dynamic response of the WES under varying wind speed conditions is illustrated with simulation and experimental results in Figures 7 and 8, respectively. The rotor speed is varied at time instant t = 1 s from sub-synchronous to super-synchronous speed (1350 to 1750 rpm). The stator-side voltage, as in Figure 7(a) tends to remain stable throughout the speed transition, indicating effective voltage regulation. The corresponding stator current in Figure 7(b) exhibits a balanced sinusoidal waveform during sub- and super-synchronous operation. The rotor-side voltage and current shown in Figure 7(c) and Figure 7(d) clearly indicate a change in magnitude and phase sequence during the transition from sub-synchronous to super-synchronous mode, reflecting the reversal of slip power. The load-side voltage and current responses in Figure 7(e) and Figure 7(f) confirm that the load is not affected by the generator-side transients and that the load is of balanced in nature. The waveform of DCLV during the speed transition is shown in Figure 7(g). The corresponding real-time results are obtained through OP4512 and are shown in Figures 8(a)–8(f) to validate the simulation outcomes. The stator voltage (Figure 8(a)) and stator current (Figure 8(b)) are seen to maintain stability, while the rotor variables (Figure 8(c) and Figure 8(d)) capture the dynamic transition accurately. The changeover in the phase sequence and the frequency changes with respect to the speed change are clearly seen in the figures. The load voltage and current (Figure 8(e) and Figure 8(f)) remain regulated, confirming that the control ensures seamless operation across operating regions.

5.2. System performance evaluation during unbalanced and non-linear load

The dynamic response of the system under unbalanced loading, that are validated through computer simulation and real-time testing, is presented in Figures 9 and 10, respectively. Also, the system performance under non-linear load, validated through simulation and real-time testing, is shown in Figures 11 and 12, respectively.

- Case 1 - Unbalanced load: A 30% load unbalance is introduced in the system with the load currents being I_{sa}= I_{sb}= 1.7 A and I_{sc}=1.19 A, respectively. With load being unbalanced, a speed change is introduced in the system at instant ‘t’ = 1 sec as, similar to previous case.
- Case 2 – Non-linear load: The non-linear load proposed in this study is three phase diode bridge rectifiers feeding a resistive load, acting as balanced non-linear load.

In both cases, the stator voltage shows slight distortion due to the imposed unbalances and non-linearity, as in Figures 9(a) and 11(a), while Figures 9(b) and 11(b) indicate the compensating stator currents that are injected by the SSSCR. The stator currents seem to be balanced sinusoids irrespective of the load nature. The rotor-side voltage and current (Figures 9(c), 11(c) and Figures 9(d), 11(d)) adapt dynamically to support compensation, and the phase sequence changeover indicates the two-directional slip-power exchange irrespective of speed and load changes. The unbalanced load voltage (Figure 9(e)) is maintained close to nominal despite a 30% unbalance, and the unbalanced load current initially reflects asymmetry before compensation (Figure 9(f)). Similarly, the non-linear load voltage and the non-linear load current (Figures 11(e) and 11(f)) exhibit the double peak nature, indicating the high non-linearity in the waveform. The distorted waveform of the DCLV under the unbalanced and non-linear load conditions is shown in Figures 9(g) and 11(g), respectively. Under these conditions, the DC-link voltage varies around its nominal value of 1150 V, increasing to approximately 1170 V and decreasing to approximately 1130 V. The real-time validation is shown in Figures 10 and 12 for both cases, respectively, wherein the stator voltage and current (Figures 10(a), 12(a) and Figures 10(b), 12(b)) remain balanced despite the speed change at instant ‘t’. The rotor responses shown in Figures 10(c), 12(c) and 10(d), 12(d) exhibit the two-directional slip-power exchange capability of the system in accordance to the speed changes, whereas, the load parameters exhibit the unbalances and non-linearity nature shown in Figures 10(e), 12(e) and 10(f), 12(f). It is observed that the unbalances and non-linearity at PCC are effectively compensated, and balanced sinusoids are maintained at the stator thereby maintaining the quality of stator power.

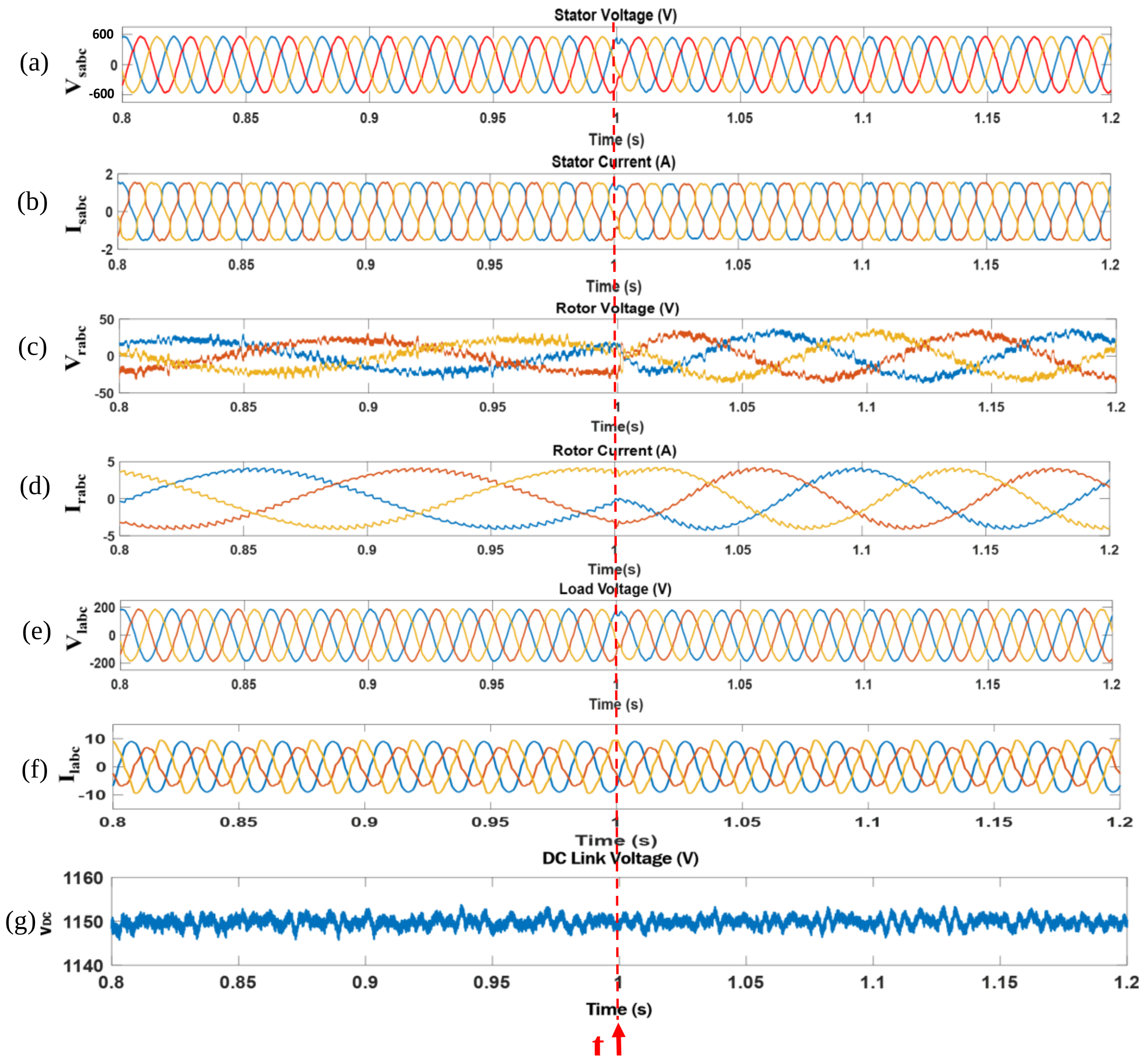

Figure 7. Response of the wind energy system during speed transition from sub-synchronous speed to super-synchronous speed at (a) stator-side voltage, (b) stator-side current, (c) rotor-side voltage, (d) rotor-side current, (e) load-side voltage, (f) load-side current, and (g) DC link voltage

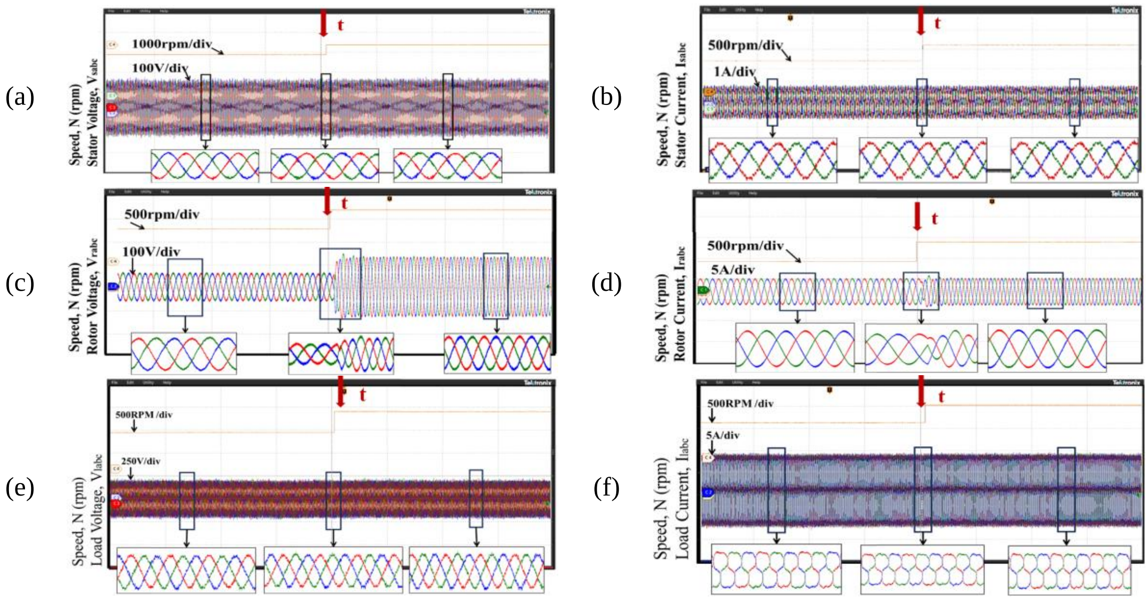

Figure 8. Response of the wind energy system during speed variation from sub-synchronous speed to super synchronous speed at (a) stator-side voltage, (b) stator-side current, (c) rotor-side voltage, (d) rotor-side current, (e) load-side voltage, and (f) load-side current

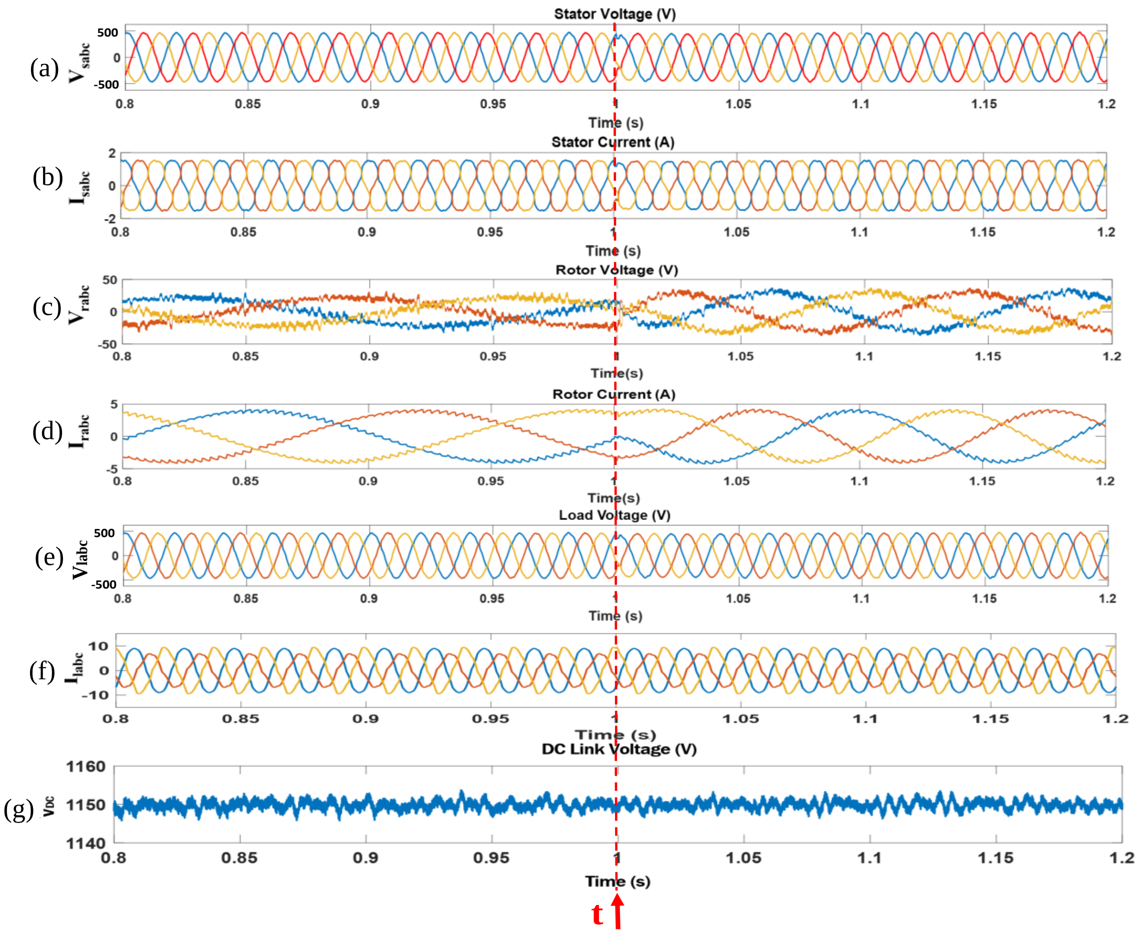

Figure 9. System response for the parameters: (a) stator-side voltage, (b) stator-side current, (c) rotor-side voltage, (d) rotor-side current, (e) load-side voltage, (f) load-side current, and (g) DC link voltage during unbalanced load conditions in the software simulation

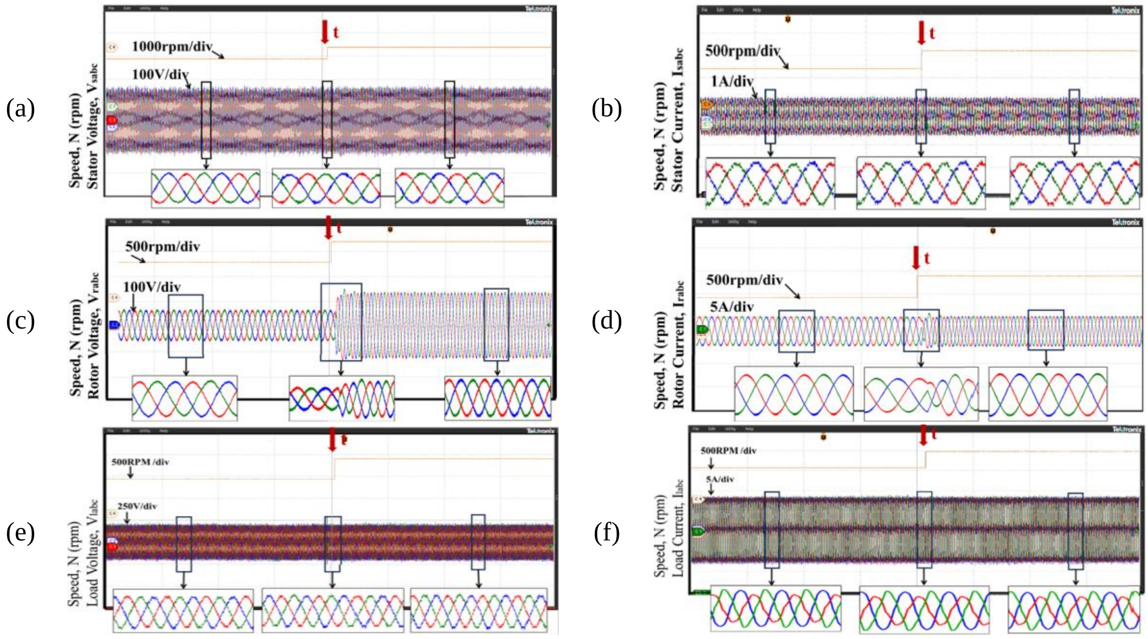

Figure 10. Real-time system response for the parameters: (a) stator-side voltage, (b) stator-side current, (c) rotor-side voltage, (d) rotor-side current, (e) load-side voltage, and (f) load-side current during unbalanced load conditions

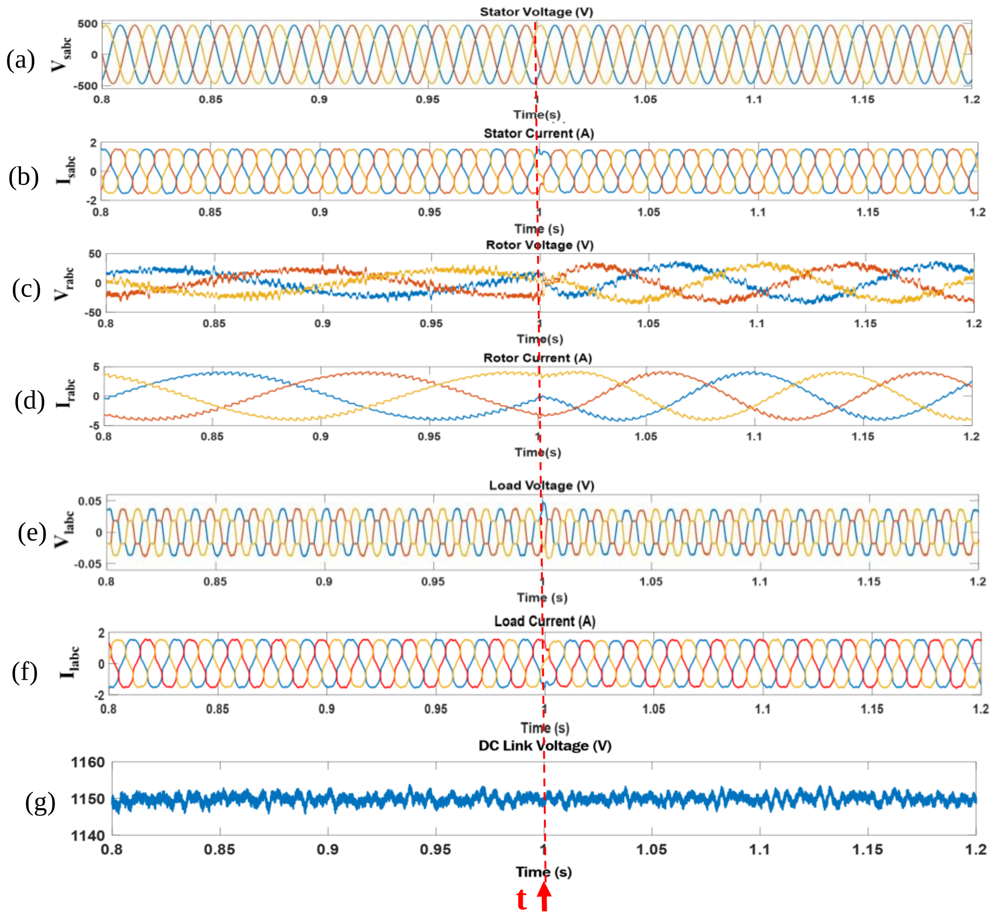

Figure 11. System response for the parameters: (a) stator-side voltage, (b) stator-side current, (c) rotor-side voltage, (d) rotor-side current, (e) load-side voltage, (f) load-side current, and (g) DC link voltage during non-linear load conditions in the software simulation

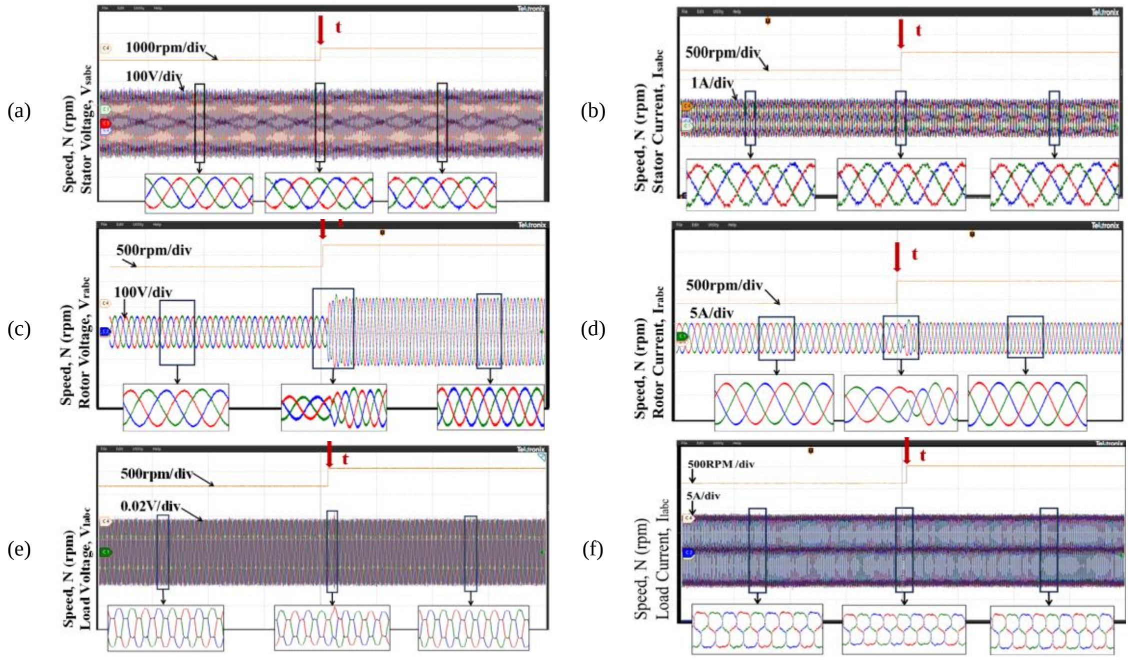

Figure 12. Real-time system response for the parameters (a) stator-side voltage, (b) stator-side current, (c) rotor-side voltage, (d) rotor-side current, (e) load-side voltage, and (f) load-side current during non-linear load conditions

5.3. Performance of the system during symmetrical and asymmetrical voltage unbalance – voltage sag and swell

The system is investigated for its performance during voltage sag and swell at PCC. The computer simulation validation is shown in Figures 13 and 14 for sag and swell respectively, and the experimentation is depicted in Figure 15.

- Case 1: voltage sag

A voltage sag of 30% is introduced between 0.5 sec and 0.7 sec (simulation), during which the line-to-line voltage at the stator drops from 575 V to 400 V, as depicted in Figure 13(a). The proposed SSSCR injects the required compensating voltage and achieves 100% sag compensation. Thereby, the PCC voltage is restored to its nominal 575 V level.

- Case 2: voltage swell

A voltage swell of 30% is introduced between 1.5 sec and 1.7 sec (simulation), during which the voltage (line-to-line) at the stator from 575 V to 750 V is depicted in Figure 14(a). The proposed SSSCR injects the required compensating voltage to counteract the voltage swell and achieves 100% swell compensation, thereby restoring the PCC voltage to its nominal value of 575 V.

- Case 3: asymmetrical unbalance – single-phase unbalance (line-ground)

In this case, a single phase is grounded, so as to exert asymmetrical unbalance. A voltage asymmetrical unbalance of 65% is introduced between 0.5 sec and 1 sec (simulation), during which the single-phase voltage (line-to-line) at the stator reduces from 575 V to 200 V is depicted in Figure 15(a).

In cases 1 and 2, the performance validation with simulation is made by exerting voltage sag and swell and asymmetrical balance at the grid side as shown in Figures 13(b), 14(b) and 15(b) and the SSSCR control injects the required voltage so as to maintain the PCC voltage stable, balanced and regulated at 575 V with the same being shown in Figures 13(c), 14(c) and 15(c) respectively. Case 3 is validated in real time alone.

The real-time validation is performed using the real-time controller OP4512, and the performance is shown in Figure 16. The grid voltage exhibits sag, swell, and asymmetrical unbalance at three different instants as in Figure 16(a). The injected/compensated voltage by the SSSCR is depicted in Figure 16(b), with the regulated PCC voltages as in Figure 16(c). The PCC current is also depicted in Figure 16(d), which is distorted owing to the fluctuations that exist in the voltages.

The quantitative results of the system, including PCC current THD, voltage regulation error, and voltage settling time, are summarized in Table 3. The obtained results demonstrate the effectiveness of the proposed compensation scheme in improving power quality. Furthermore, the proposed scheme enhances voltage regulation under both nonlinear and unbalanced loading conditions.

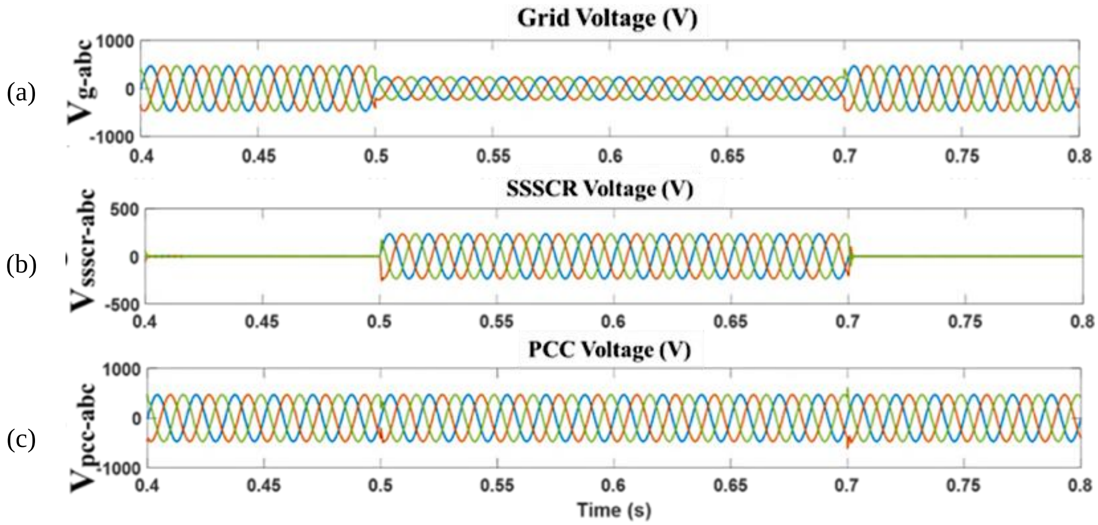

Figure 13. System's response during symmetrical voltage unbalance – voltage sag: (a) grid-side voltage, (b) SSSCR voltage, and (c) PCC voltage

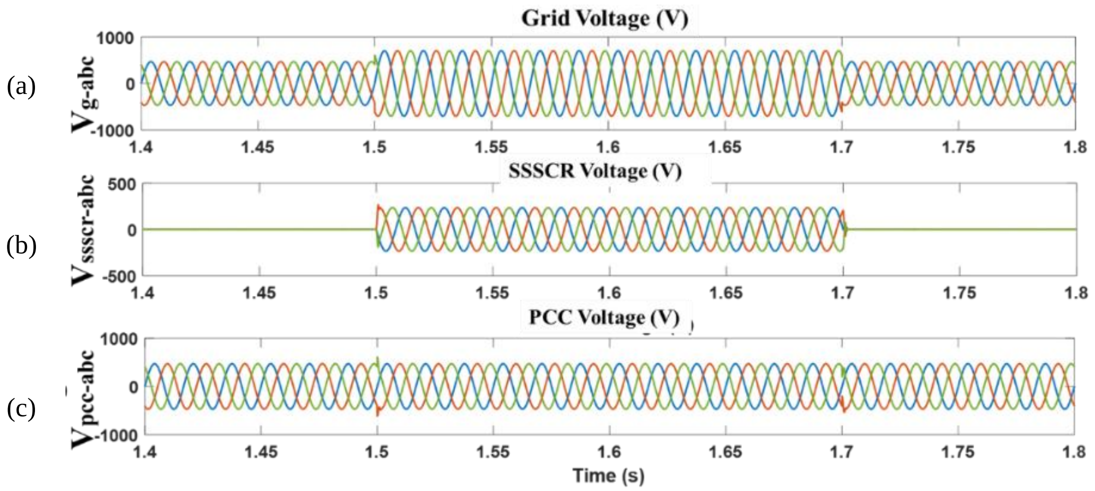

Figure 14. System's response during symmetrical voltage unbalance – voltage swell: (a) grid-side voltage, (b) SSSCR voltage, and (c) PCC voltage

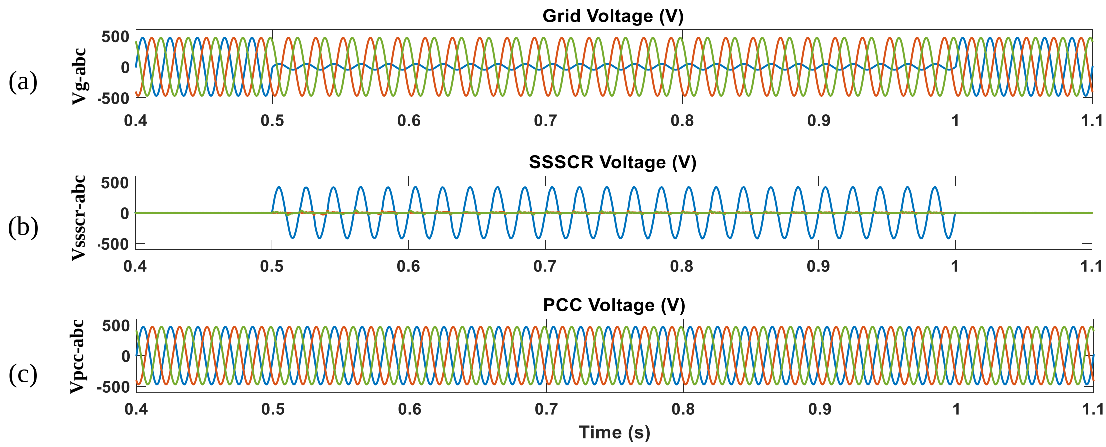

Figure 15. System's response during asymmetrical voltage unbalance: (a) grid-side voltage. (b) SSSCR voltage, and (c) PCC voltage

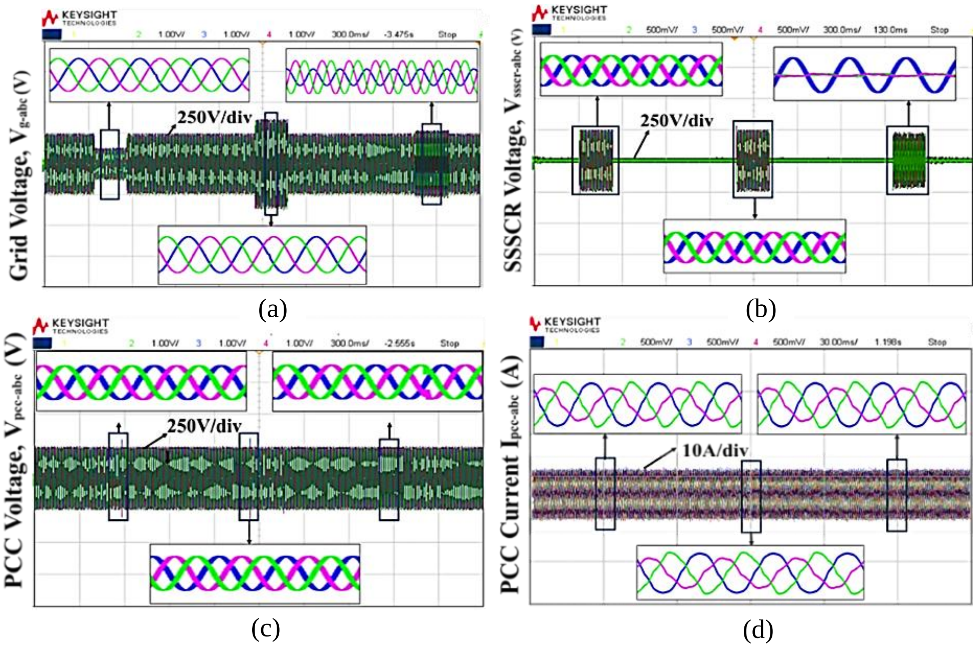

Figure 16. System's response during symmetrical unbalance and asymmetrical unbalance: (a) grid-side voltage, (b) SSSCR voltage, (c) voltage at PCC, and (d) current at PCC

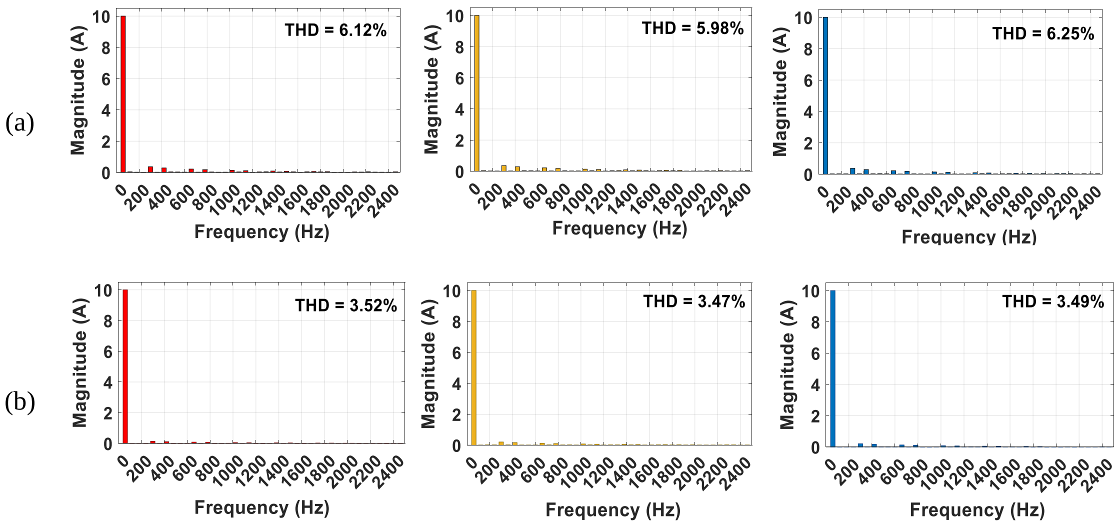

Figure 17. THD spectrums of the PCC current during: (a) non-linear load case and (b) unbalanced load case

5.4. Limitations and future directions

Certain limitations remain in the present study. Although the proposed control framework has been validated through MATLAB/Simulink- based analysis and real-time validation, a full-scale physical hardware prototype was not considered. Such an implementation would provide further insight into practical effects such as converter switching delays, sensor inaccuracies, communication and computational latencies, parameter uncertainties, thermal limitations, and non-ideal switching behavior.

The proposed control strategy was primarily evaluated under voltage sag, voltage swell, unbalanced-load, and nonlinear-load conditions. More severe operating conditions, including three-phase faults, cascading disturbances, large grid-frequency excursions, and prolonged low-voltage ride-through (LVRT) events, were not investigated in the present study. These conditions may impose higher transient stresses on the converters and DC-link and may require additional protection and energy-balancing mechanisms.

In addition, the coordinated operation of the RSCR and SSSCR introduces interactions among the converter controllers, DC-link dynamics, PLL, and grid-side disturbances. Therefore, controller parameters optimized for the investigated operating conditions cannot be directly transferred to all grid strengths and power ratings. Further studies involving adaptive gain tuning, grid-strength variations, and systematic stability assessment are required.

Future research will focus on adaptive and intelligent control techniques based on artificial intelligence and machine learning- based control techniques to improve dynamic response and disturbance-rejection capability. Experimental implementation using real-time digital controllers and power-converter prototypes will also be considered to further verify the practical applicability of the proposed scheme. Furthermore, the proposed framework can be extended to offshore wind farms, hybrid renewable-energy systems, and microgrid applications involving both grid-forming and grid-following converter operation.

Table 3. Quantitative analysis of the system during nonlinear load and unbalanced load conditions

Cases	Performance metric	Without proposed control	With proposed control
Non-linear load	R-phase	8.21%	6.12%
	Y-phase	8.05%	5.98%
	B-phase	8.32%	6.25%
	Overall THD	8.19%	6.12%
	DC link voltage regulation error	9	3
	DC link voltage – settling time	240 ms	120 ms
Unbalanced load	R-phase	5.82%	3.52%
	Y-phase	5.36%	3.47%
	B-phase	5.38%	3.49%
	Overall THD	5.52%	3.49%
	DC link voltage regulation error	8	3
	DC link voltage – settling time	210 ms	100 ms
	Voltage unbalance factor	3.12	0.8
Speed transition	DC link voltage - Overshoot	2.61%	0.02%
	DC link voltage deviation	5.49%	1.24%

5.5. Practical scalability

The proposed RSCR–SSSCR coordinated control philosophy is applicable to higher-power DFIG-based WESs; however, direct transfer of the controller parameters and converter ratings from the present implementation to a higher-power system is not recommended. At MW-scale ratings, the semiconductor devices, series injection transformer, filters, and associated thermal-management systems must be appropriately sized according to the required compensation voltage, load current, and transient operating conditions. Higher-power implementations may also require multilevel converter topologies to reduce device voltage stress and switching-related losses while maintaining the required power-quality performance.

The converter rating is particularly important during severe voltage disturbances because the SSSCR must generate the required series compensation voltage without exceeding its voltage, current, and thermal limits. Similarly, transient active-power exchange between the converters must be considered in the design of the DC-link capacitor and its protection and energy-balancing mechanisms. Therefore, DCLV regulation, converter protection, and energy management should be re-evaluated when the proposed architecture is scaled to higher power levels.

At larger wind-farm ratings, the interaction between the RSCR, SSSCR, PLL, filters, and grid impedance may also become more significant, particularly under weak-grid conditions. Consequently, controller gains, bandwidths, and stability margins should be systematically re-tuned using the corresponding per-unit machine, converter, filter, and grid parameters rather than directly adopting the values used in the present study. Measurement uncertainties, computational delays, communication delays, and controller interactions should likewise be included in a full-scale implementation assessment.

In addition to the technical considerations, practical deployment requires compliance with applicable grid-code requirements concerning low-voltage ride-through, reactive-power support, voltage regulation, and harmonic distortion. The economic feasibility of the proposed architecture should also be evaluated by considering the ratings of the SSSCR, injection transformer, DC-link capacitor, semiconductor devices, protection system, and associated control hardware. Therefore, the proposed architecture demonstrates a promising scalable control concept, while detailed converter sizing, protection coordination, cost-benefit analysis, and full-scale experimental validation remain necessary before industrial deployment.

6. CONCLUSION

This paper addresses the simultaneous voltage injection and load compensation framework for a DFIG-based WES operating under weak-grid conditions. The proposed architecture integrates a rotor-side converter (RSCR) and a stator-side series converter (SSSCR) through a common DC-link. The RSCR employs coordinated cascaded voltage-current control loops to facilitate two-directional rotor slip-power exchange and regulation of stator parameters over a wide range of wind speeds. The SSSCR is controlled using a current-controlled reference current generation technique, and it functions as a series voltage regulator capable of compensating for voltage disturbances and load-induced power quality issues at the PCC. Alongside, the WES addresses multiple objectives: i) two-directional slip-power exchange, ii) load compensation, iii) regulation of voltage and frequency at the stator, iv) reduced THD, and v) enhanced voltage support during sag/swell – all with a single unified system/approach. The proposed control strategy is validated through detailed MATLAB/Simulink based computer simulation and real-time hardware-in-the-loop (HiL) assessment using the OPAL-RT OP4512 platform. The real time results are seen to closely match with the simulation findings demonstrating the practical feasibility of the proposed control and the key findings of the work are summarized as: i) seamless transition between sub-synchronous and super-synchronous operating regimes with stable stator voltage and balanced current profiles, ii) under unbalanced and nonlinear load conditions, the proposed controller effectively compensated load asymmetry and restored balanced operating conditions at the PCC and also mitigated waveform distortions and maintained acceptable power quality levels, iii) the voltage sag and swell are addressed at PCC through the injection of required series voltage and the PCC voltage is restored to its nominal value.

ACKNOWLEDGMENT

The authors gratefully acknowledge the Centre of Electric Mobility (CEM), SRM Institute of Science and Technology, Kattankulathur, for providing access to the OPAL-RT real-time simulation platform (OP4512), which was instrumental in the validation process. The authors also acknowledge the Control, Energy and Testing Laboratory, SRM Institute of Science and Technology, Kattankulathur, for its in-kind support.

FUNDING INFORMATION

This work was supported by the Department of Science and Technology – ASEAN India S&T Development Fund (DST-AISTDF), New Delhi, under Grant No. CRD/2022/000669.

AUTHOR CONTRIBUTIONS STATEMENT

This journal uses the Contributor Roles Taxonomy (CRediT) to recognize individual author contributions, reduce authorship disputes, and facilitate collaboration.

Name of Author	C	M	So	Va	Fo	I	R	D	O	E	Vi	Su	P	Fu
Preethicaa Ramesh		✓	✓	✓	✓		✓		✓					
Sowmmiya Uthayakumar	✓	✓	✓	✓	✓	✓	✓			✓		✓	✓	
Tole Sutikno	✓			✓	✓		✓			✓		✓	✓	
Vigna Kumaran Ramachandaramurthy	✓			✓	✓		✓			✓		✓	✓	

C : **C**onceptualization
M : **M**ethodology
So : **So**ftware
Va : **Va**lidation
Fo : **Fo**rmal analysis
I : **I**nvestigation
R : **R**esources
D : **D**ata Curation
O : Writing - **O**riginal Draft
E : Writing - Review & **E**diting
Vi : **Vi**sualization
Su : **Su**pervision
P : **P**roject administration
Fu : **Fu**nding acquisition

CONFLICT OF INTEREST STATEMENT

The authors confirm that they have no conflicts of interest to disclose.

DATA AVAILABILITY

The datasets and simulation models generated and analyzed during the current study are not publicly available due to institutional restrictions.

REFERENCES

[1] R. D. Shukla and R. K. Tripathi, "A novel voltage and frequency controller for standalone DFIG based Wind energy conversion system," *Renewable and Sustainable Energy Reviews*, vol. 37, pp. 69–89, 2014, doi: 10.1016/j.rser.2014.04.069.

[2] M. A. Mostafa, E. A. El-Hay, and M. M. ELkholy, "Recent trends in wind energy conversion system with grid integration based on soft computing methods: comprehensive review, comparisons and insights," *Archives of Computational Methods in Engineering*, vol. 30, no. 3, pp. 1439–1478, 2023, doi: 10.1007/s11831-022-09842-4.

[3] S. Xiao, H. Geng, H. Zhou, and G. Yang, "Analysis of the control limit for rotor-side converter of doubly fed induction generator-based wind energy conversion system under various voltage dips," *IET Renewable Power Generation*, vol. 7, no. 1, pp. 71–81, 2013, doi: 10.1049/iet-rpg.2011.0348.

[4] V. C. Ganti, B. Singh, S. K. Aggarwal, and T. C. Kandpal, "DFIG-based wind power conversion with grid power leveling for reduced gusts," *IEEE Transactions on Sustainable Energy*, vol. 3, no. 1, pp. 12–20, 2012, doi: 10.1109/TSTE.2011.2170862.

[5] A. A. Tanvir, A. Merabet, and R. Beguenane, "Real-time control of active and reactive power for doubly fed induction generator (DFIG)-based wind energy conversion system," *Energies*, vol. 8, no. 9, pp. 10389–10408, 2015, doi: 10.3390/en80910389.

[6] S. Qin, M. Yang, X. Zhang, Z. Ma, J. Zhao, and D. Xu, "Voltage disturbance compensation based on impedance modeling of DFIG under weak grid," *International Journal of Electrical Power and Energy Systems*, vol. 131, 2021, doi: 10.1016/j.ijepes.2021.107062.

[7] G. S. Chawda and A. G. Shaik, "A reactive power-based adaptive approach for synchronization of DFIG into the weak grid to support existing WE infrastructure," *International Journal of Electrical Power and Energy Systems*, vol. 157, 2024, doi: 10.1016/j.ijepes.2024.109850.

[8] J. Vega-Herrera *et al.*, "AC voltage and reactive power control in DFIG-based wind farms: A comparative study for mitigating sub-synchronous resonance in compensated and weak networks," *Energy Reports*, vol. 14, pp. 566–578, 2025, doi: 10.1016/j.egyr.2025.06.005.

[9] V. P. Suppioni, A. P. Grilo, and J. C. Teixeira, "Improving network voltage unbalance levels by controlling DFIG wind turbine using a dynamic voltage restorer," *International Journal of Electrical Power and Energy Systems*, vol. 96, pp. 185–193, 2018, doi: 10.1016/j.ijepes.2017.10.002.

[10] H. Zhang, G. Xiao, Z. Lu, and Y. Chai, "Reduce response time of single-phase dynamic voltage restorer (dvr) in a wide range of operating conditions for practical application," *IEEE Journal of Emerging and Selected Topics in Power Electronics*, vol. 10, no. 2, pp. 2101–2113, 2022, doi: 10.1109/JESTPE.2021.3119947.

[11] N. K. S. Naidu and B. Singh, "Grid-interfaced DFIG-based variable speed wind energy conversion system with power smoothening," *IEEE Transactions on Sustainable Energy*, vol. 8, no. 1, pp. 51–58, 2017, doi: 10.1109/TSTE.2016.2582520.

[12] A. Heenkenda, A. Elsanabary, M. Seyedmahmoudian, S. Mekhilef, A. Stojcevski, and N. F. A. Aziz, "Unified power quality conditioners based different structural arrangements: a comprehensive review," *IEEE Access*, vol. 11, pp. 43435–43457, 2023, doi: 10.1109/ACCESS.2023.3269855.

[13] R. Gupta, A. Ghosh, and A. Joshi, "Performance comparison of VSC-based shunt and series compensators used for load voltage control in distribution systems," *IEEE Transactions on Power Delivery*, vol. 26, no. 1, pp. 268–278, 2011, doi: 10.1109/TPWRD.2010.2076341.

[14] U. Sowmmiya, M. S. Keerthana, A. Karthikeyan, and K. Padmanathan, "Dual converters coupled to thermal grid for simultaneous control on regulation and compensation in a hybrid AC-DC network," *Electric Power Components and Systems*, 2024, doi: 10.1080/15325008.2024.2313578.

[15] N. Zanib *et al.*, "Analysis and power quality improvement in hybrid distributed generation system with utilization of unified power quality conditioner," *CMES - Computer Modeling in Engineering and Sciences*, vol. 134, no. 2, pp. 1105–1136, 2023, doi: 10.32604/cmes.2022.021676.

[16] J. X. Jin, R. H. Yang, R. T. Zhang, Y. J. Fan, Q. Xie, and X. Y. Chen, "Combined low voltage ride through and power smoothing control for DFIG/PMSG hybrid wind energy conversion system employing a SMES-based AC-DC unified power quality conditioner," *International Journal of Electrical Power and Energy Systems*, vol. 128, 2021, doi: 10.1016/j.ijepes.2020.106733.

[17] B. Khan *et al.*, "Power quality improvement of microgrids using unified power quality conditioner (UPQC): A scoping review," *Electric Power Systems Research*, vol. 253, 2026, doi: 10.1016/j.epsr.2025.112573.

[18] B. P. Babu and V. Indragandhi, "A review on dynamic voltage restorer in power systems concerned to the issues of power quality," *IOP Conference Series: Materials Science and Engineering*, vol. 623, no. 1, 2019, doi: 10.1088/1757-899X/623/1/012015.

[19] R. Sitharthan, C. K. Sundarabalan, K. R. Devabalaji, S. K. Nataraj, and M. Karthikeyan, "Improved fault ride through capability of DFIG-wind turbines using customized dynamic voltage restorer," *Sustainable Cities and Society*, vol. 39, pp. 114–125, 2018, doi: 10.1016/j.scs.2018.02.008.

[20] K. Jiang, L. Li, Z. He, and D. Liu, "Stability limit analysis of DFIG connected to weak grid in DC-link voltage control timescale," *Electronics (Switzerland)*, vol. 14, no. 15, 2025, doi: 10.3390/electronics14153022.

[21] M. Mokhber-Yengikand, S. Tohidi, M. R. Feyzi, and M. H. Ravanji, "H∞-based current control for mitigating high-frequency resonance in parallel compensated weak grid connected DFIG wind turbines," *Electric Power Systems Research*, vol. 254, 2026, doi: 10.1016/j.epsr.2025.112682.

[22] H. Yuan, D. Wang, and X. Zhou, "Frequency support of DFIG-based wind turbine via virtual synchronous control of inner voltage vector," *Electric Power Systems Research*, vol. 225, 2023, doi: 10.1016/j.epsr.2023.109823.

[23] A. Mishra, P. M. Tripathi, and K. Chatterjee, "A review of harmonic elimination techniques in grid connected doubly fed induction generator based wind energy system," *Renewable and Sustainable Energy Reviews*, vol. 89, pp. 1–15, 2018, doi: 10.1016/j.rser.2018.02.039.
[24] M. H. Shaabani, B. Vahidi, and M. J. Jalilian, "Enhanced LVRT capability in a DFIG-based wind-powered electrical system using machine learning-based adaptive PI controller under various grid voltage dip conditions," *Sustainable Computing: Informatics and Systems*, vol. 51, 2026, doi: 10.1016/j.suscom.2026.101400.
[25] G. N. González, C. H. De Angelo, and D. A. Aligia, "A control strategy for DFIG-based systems operating under unbalanced grid voltage conditions," *International Journal of Electrical Power and Energy Systems*, vol. 142, 2022, doi: 10.1016/j.ijepes.2022.108273.
[26] U. Karaagac, I. Kocar, J. Mahseredjian, L. Cai, and Z. Javid, "STATCOM integration into a DFIG-based wind park for reactive power compensation and its impact on wind park high voltage ride-through capability," *Electric Power Systems Research*, vol. 199, 2021, doi: 10.1016/j.epsr.2021.107368.
[27] A. Mohanty, M. Viswavandya, P. K. Ray, and S. Patra, "Stability analysis and reactive power compensation issue in a microgrid with a DFIG based WECS," *International Journal of Electrical Power and Energy Systems*, vol. 62, pp. 753–762, 2014, doi: 10.1016/j.ijepes.2014.05.033.
[28] V. Sohoni, S. C. Gupta, and R. K. Nema, "A critical review on wind turbine power curve modelling techniques and their applications in wind based energy systems," *Journal of Energy*, vol. 2016, pp. 1–18, 2016, doi: 10.1155/2016/8519785.
[29] V. Akhmatov, "Variable-speed wind turbines with doubly-fed induction generators. Part I: Modelling in dynamic simulation tools," *Wind Engineering*, vol. 26, no. 2, pp. 85–108, 2002, doi: 10.1260/030952402761699278.
[30] Y. Jiang, Y. Tian, and Y. Li, "DC-link capacitor current observation based stability enhancement control for back-to-back converter," *IET Power Electronics*, vol. 15, no. 6, pp. 558–570, 2022, doi: 10.1049/pel2.12249.
[31] F. Blaabjerg and Z. Chen, "Power electronics for modern wind turbines," *Synthesis Lectures on Power Electronics*, vol. 1, pp. 1–68, 2005, doi: 10.2200/S00014ED1V01Y200602PEL001.
[32] N. G. Hingoranl, L. Gyugyi, and M. E. El-Hawary, "Understanding FACTS: Concepts and technology of flexible ac transmission systems," *Understanding FACTS: Concepts and Technology of Flexible AC Transmission Systems*, pp. 1–432, 1999, doi: 10.1109/9780470546802.
[33] M. Sylvain, "OP4512 System Description," OPAL-RT Technologies, Inc. Accessed: Aug. 17, 2026.[Online].Available: https://opal-rt.atlassian.net/wiki/spaces/PHDGD/pages/144658809/OP4512+System+Description

BIOGRAPHIES OF AUTHORS

Preethicaa Ramesh is a junior research fellow (JRF) at SRM Institute of Science and Technology, Kattankulathur, Chengalpattu, Tamil Nadu, India, where she has been working since June 2024. She previously served as an assistant professor at Nadar Saraswathi College of Engineering and Technology, India, from August 2021 to May 2022. She worked as an engineer at JEF Techno Solutions Pvt. Ltd., Bengaluru, India, from September 2017 to August 2018 and as a graduate apprentice trainee at Schneider, Chennai, Tamil Nadu, India, from July 2016 to January 2017. She completed her Master of Engineering (M.E.) degree in power engineering and management at Anna University, Chennai, in 2020. She obtained her postgraduate diploma in transmission and distribution from the National Power Training Institute in 2017 and her Bachelor of Engineering (B.E.) degree in electrical and electronics engineering from Panimalar Institute of Technology, Chennai. Her research interests include power generation, power electronics, smart grids, wind energy, and related areas. She can be contacted at email: pr7886@srmist.edu.in.

Sowmmiya Uthayakumar is an associate professor at SRM Institute of Science and Technology, Kattankulathur, with more than 15 years of academic and research experience. She received her B.E. degree in electrical and electronics engineering and her M.E. degree specializing in power electronics and drives from Anna University, Chennai. She also received her Ph.D. degree from the College of Engineering, Guindy, Anna University, Chennai. She was awarded a postdoctoral fellowship under the Young Scientist Fellowship Scheme of TNSCST at the National Institute of Technology Karnataka. Her research interests include renewable energy integration, condition monitoring, power transfer in wind energy systems, and power quality challenges in propulsion systems. She has published numerous articles in refereed, science-indexed international journals and conference proceedings and has contributed several book chapters to indexed volumes. She also serves as the branch counsellor for the SRM-IAEMP Student Chapter. She has received several honors, including the Wenlock Endowment Scheme from Anna University, the Marina Labs Young Researcher Award, the Institute of Scholars Research Excellence Award, and the Strategies in Green Excellence Award from CENR, SRM. She can be contacted at email: sowmmiyu@srmist.edu.in.

Tole Sutikno is a full professor in the Department of Electrical Engineering at Universitas Ahmad Dahlan, Yogyakarta, Indonesia. He has served in this role since 2023, after his appointment as associate professor in 2008. He received his bachelor's degree from Universitas Diponegoro in 1999, master's degree from Universitas Gadjah Mada in 2004, and Ph.D. in Electrical Engineering from Universiti Teknologi Malaysia in 2016. His doctoral research focused on advanced digital power electronics and intelligent control systems. From 2016 to 2021, he served as Director of the Institute for Scientific Publishing and Publications at Universitas Ahmad Dahlan, where he led initiatives in research visibility, journal management, and international scholarly collaboration. He is the founding leader of the Embedded Systems and Power Electronics Research Group, which collaborates with national and international institutions in fault-tolerant embedded systems, FPGA-based control, and renewable energy integration. His research interests include digital design, industrial electronics, motor drives, robotics, intelligent systems, AI-based automation, embedded systems, power electronics, FPGA applications, and digital libraries. His work focuses on practical applications in industrial and healthcare contexts. He has been listed among the Top 2% of Scientists Worldwide by Stanford University and Elsevier BV from 2021 to the present, based on standardized citation indicators across scientific disciplines. He can be contacted at email: tole@te.uad.ac.id.

Vigna Kumaran Ramachandaramurthy received his bachelor's degree in electrical and electronics engineering from the University of Manchester Institute of Science and Technology (UMIST), U.K., in 1998 under the Malaysian Government Scholarship, and his Ph.D. degree in electrical engineering from UMIST in 2001. He began his career in 2002 as an electrical engineer with Tenaga Nasional Berhad, Malaysia's national electricity utility. In 2005, he joined Universiti Tenaga Nasional (UNITEN), where he is currently a professor at the Institute of Power Engineering. He is a Chartered Engineer registered with the Engineering Council of the U.K. and a Professional Engineer registered with the Board of Engineers Malaysia. He also serves as a principal consultant for Tenaga Nasional Berhad, Malaysia's largest electricity utility. He is a member of several professional organizations, with research interests including power systems, renewable energy, energy storage, power quality, electric vehicles, and rural electrification. He has participated in numerous industrial consultancy projects and supervised more than 100 postgraduate candidates. He has received several awards for research and leadership, including the IET Mike Sargeant Award, the IEM Young Engineers Award, and the Best Researcher Award at UNITEN. He can be contacted at email: vigna@uniten.edu.my.